Universidad Autónoma de Madrid
Escuela politécnica superior

Máster Universitario en Investigación e Innovación en TIC (i2-TIC)

Trabajo Fin de Máster

COMPUTATIONAL MODELLING OF THE DEEP-SUPERFICIAL FUNCTIONALITY ON THE CA1 HIPPOCAMPAL REGION

Autora: Andrea Claudia Navas Olivé
Directora: Liset Menéndez de la Prida
Tutor: José Dorronsoro Ibero

June 2017

COMPUTATIONAL MODELLING OF THE DEEP-SUPERFICIAL FUNCTIONALITY ON THE CA1 HIPPOCAMPAL REGION

Autora: Andrea Claudia Navas Olivé
Directora: Liset Menéndez de la Prida
Tutor: José Dorronsoro Ibero

Instituto Cajal - CSIC
Escuela Politécnica Superior
Universidad Autónoma de Madrid
June 2017

Abstract

Resumen

Las oscilaciones theta (4-12Hz) están consideradas el modo on-line más importante del hipocampo durante la navegación espacial. Durante la codificación, actúa como un canal de información entre regiones del hipocampo para las diferentes fases del ritmo. Las corrientes sinápticas que subyacen en la región CA1 hipocampal se generan en CA3 y corteza entohrinal junto con inhibición local, pero los mecanismos de la fase preferente de disparo aún son desconocidos. Estudios recientes sugieren que los microcircuitos hipocampales son mucho más complejos de lo que originalmente se pensaba. Por ejemplo, en trabajos del laboratorio receptor se vio que la región CA1 está organizada en subcapas de células principales superficiales y profundas, presentando características específicas en los ritmos hipocampales.

Los modelos computacionales realistas de redes neuronales son una herramienta básica en neurociencia. El formalismo de Hodgkin-Huxley ofrece una oportunidad única para simular la actividad eléctrica de neuronas multicompartimentales y circuitos. En este trabajo, presentamos un modelo computacional de una columna cilíndrica de neuronas piramidales realistas superficiales y profundas que incorpora características morfológicas y sinápticas específicas en respuesta a la excitación de la región CA3. A lo largo del proyecto se persiguen los siguientes objetivos: 1) Generar una simulación realista en el entorno NEURON que permita incluir morfologías de células piramidales de CA1 tanto reconstruidas por el laboratorio receptor, como de bases de datos libres como es NeuroMorpho; 2) Configurar las propiedades intrínsecas y sinápticas de las células piramidales de CA1; 3) Simular de forma realista el potencial eléctrico extracelular generado por las neuronas individuales, y por un pequeño cilindro de neuronas realistas; y 4) Implementar simulaciones preliminares del ritmo theta hipocampal.

El modelo reproduce satisfactoriamente algunos de los aspectos biofísicos y electrofisiológicos de las células piramidales de CA1 registrados *in vivo*. El papel de la morfología neuronal, la arborización dendrítica, el diámetro dendrítico y el factor de escala de las espinas dendríticas en la actividad eléctrica del soma fue evaluada con detalle. Fue así mismo evaluado el efecto de los canales catiónicos HCN en el potencial de membrana y la normalización de la atenuación electrotónica, dado su gran impacto en las propiedades resonantes de las células hipcampales durante el ritmo theta. Como segunda parte de este proyecto, se simuló el potencial eléctrico extracelular emergente de las neuronas individuales ante estimulación sináptica. Gracias a la flexibilidad del código, el modelo de neurona individual pudo ser escalado fácilmente, generando de esta manera el potencial eléctrico extracelular de un cilindro de neuronas. Finalmente, se obtuvieron resultados preliminares del ritmo theta hipocampal como una prueba de concepto para un modelo más ambicioso de la región CA1 hipocampal.

Palabras clave

Células piramidales de CA1, profunda superficial, formalismo de Hodgkin-Huxley, theta, oscilaciones, NEURON, NeuroMorpho

Abstract

Theta oscillations (4-12Hz) are considered a major on-line mode of the hippocampus during spatial navigation. During encoding, theta acts to channel information flow between regions across different oscillatory phases. The underlying synaptic currents in CA1 are generated by the CA3 and entorhinal inputs in interaction with local inhibition, but specific mechanisms of phase preference firing are still unknown. Remarkable, emerging data now sugggest that this hippocampal microcircuit is much more complex than originally thought. For instance, work from the host lab have shown that CA1 region is organized in sublayers, with deep and superficial principal cells displaying specific features during ongoing hippocampal rhythms.

Realistic computational models of neuronal networks are a basic tool in neuroscience research. The Hodgkin-Huxley formalism offers a unique opportunity to simulate the electrical activity of multi-compartement neurons and circuits. Here, we present a computational model of a cylindrical column made up of realistic superficial and deep CA1 pyramidal neurons that incorporates specific morphological and synaptic features in response to inputs from the CA3 region. Along this project we pursue the following goals: 1) To develop a realistic simulation environment in NEURON that allows for including realistic CA1 pyramidal cell morphologies recorded from the host laboratory as well as from open-source databases such as NeuroMorpho; 2) To set basic intrinsic and synaptic properties of CA1 pyramidal cells; 3) To realistically simulate the extracellular local field potential (LFP) generated by invididual neurons and by a small cylinder of realistic neurons and 4) To implement preliminary simulations of the hippocampal theta rhythm.

The model successfully reproduces some biophysical and electrophysiological aspects of CA1 pyramidal cells recorded in vivo. The role of neuronal morphology, dendritic branching and diameter and spine scaling factors in somatic electrical activity was specifically evaluated. In addition, the effect of cationic channels HCN on resting membrane potential and normalization of electrotonic attenuation was also validated given their major role in theta resonant properties of hippocampal cells. In a second part of the project, the LFP emerging from individual neurons after synaptic stimulation was simulated. Thanks to the flexibility of the code, the single-cell model was easily escalated and LFP signals from a cylinder of neurons was generated. Finally, preliminary results of the hippocampal theta rhythm were obtained as a proof-of-concept for a more ambitious realistic model of the CA1 hippocampal region.

Key words

CA1 pyramidal cells, deep, superficial, Hodgkin-Huxley formalism, theta, oscillations, NEURON, NeuroMorpho

Acknowledgements

Agradezco profundamente al laboratorio de Circuitos Neuronales del Instituto Cajal el haberme ofrecido esta increíble oportunidad, por haber puesto a mi disposición su brillante experiencia e iniciarme no sólo en el camino del conocimiento y la ciencia que tan bien labrado tienen, sino en el de la cooperación y la amistad. Agradezco en especial a Liset su guía, admirable, fuerte, y es una suerte poder tener una fuente de inspiración como ella tan cerca; a Jose Manuel por su generosa ayuda en los momentos más críticos de este trabajo; e indudablemente a Manu por su... todo, en realidad, su confianza en mí, motivación, su hambre de conocimiento y su alegría desbordante.

Por supuesto, agradezco cada minuto de mi trabajo a mi familia, mi querida hermana Berta, que inunda el aire que le rodea de una creatividad inalcanzable, y con la que espero compartir los frutos que vamos sembrando; a mi padre, cuyos diversos intereses modelaron desde mi primer aliento la persona que soy ahora; y especialmente a la mejor de las madres, mi más preciado modelo, de quien más tengo que aprender y a quien le agradezco toda mi vida.

Finalmente, por encima de todo, con quien no podría estar escribiendo estas líneas, mi adorado Roy, por su persistente apoyo, su paciencia, su infinito cariño, quien de la mano me arrastró desde los oscuros abismos al cielo inmenso.

Contents

Figure Index

Glossary of acronyms

- **DG**: Dentate Gyrus
- **EC**: Entorhrinal Cortex
- **CA**: Cornu Ammonis
- **SO**: Stratum Oriens
- **SP**: Stratum Pyramidale
- **SR**: Stratum Radiatum
- **SLM**: Stratum Lacunosum Moleculare
- **PC**: Pyramidal Cell
- $\mathbf{PC_{Sup}}$: Pyramidal Superficial Cell
- $\mathbf{PC_{Deep}}$: Pyramidal Deep Cell
- **PVbc**: Parvalbumin-inmunoreactive Basket Cell
- **O-LM**: Oriens-Lacunosum-Moleculare
- **CCKbc**: Cholecystokinin-inmunoreactive Basket Cell
- **LFP**: Local Field Potential
- **CSD**: Current Density Source
- **LSA**: Line Source Approximation
- **HCN**: Hyperpolarization-activated Cyclic Nucleotide-gated
- **EPSP**: Excitatory Post-Synaptic Potential
- **AIS**: Axon Initial Segment

1 Introduction

1.1 Motivation and goals

What determines the extraordinary computing capability of the brain? Despite of great progress formalizing basic computational rules in artificial neural networks, the flexibility and operability of simple animals' brain highly outperforms that of the machine. A fundamental property of electrical brain activity is its rhythmic structure linked to cognitive demands (as attention) and physiological challenges (as sleep) [Buzsáki and Moser, 2013]. Surprisingly, the frequency of these rhythms remains extraordinary preserved across species, suggesting its origin in microcircuits of few hundreds of thousands of neurons [Buzsáki and Moser, 2013].

One of the most studied brain rhythm is the *theta* rhythm. Theta (4-12 Hz) is considered the "on-line" status of the hippocampus, a highly rhythmic activity that acts as a global synchronizer mechanism for encoding and information processing [Hasselmo et al., 2002]. During a theta cycle different neuronal populations of the hippocampus fire sequentially: each one at a distinct preferred phase [Klausberger and Somogyi, 2008]. Moreover, it has been recently discovered that pyramidal neurons of the CA1 hippocampal region, generally considered a homogeneous population, can be classified into deep and superficial: not only each cell type shows a different preferred phase along theta cycles [Mizuseki et al., 2011], but also a different response in other hippocampal rhythm, sharp wave-ripples, an oscillation associated to the consolidation of memory [Valero et al., 2015]. Understanding how this coordination holds up hippocampal functions as spatial navigation and memory, is a major question in the field [O'Keefe and Recce, 1993, Hasselmo et al., 2002, Montgomery and Buzsáki, 2007, Mizuseki et al., 2009, Bieri et al., 2014].

Preferred theta phase presumably results from the hippocampal microcircuit itself, i.e. how the different population are connected would determine the firing order along theta [Klausberger and Somogyi, 2008]. Excitatory synaptic connections increase the probability of postsynaptic activity, while inhibitory synapses act to reduce it. Complex circuitries that combine excitation and inhibition can introduce different delays in the activity of each neuronal population, therefore producing the distinct preferred phases observed. Hence the study of the hippocampal microcircuit is essential to understand how coordination is achieved by brain rhythms.

Nowadays, however, there are some limitations in the experimental techniques that hamper a complete analysis of these hippocampal circuits; by instance, dendritic recordings are extremely

difficult, but critical as dendrites receive most of synaptic inputs [Shah, 2013]; or characterizing the contribution of each neural population on pyramidal cells, as specific markers are not yet available. The value of a computational realistic model that simulates the hippocampal circuitry clear shows up, as it allows to access the dynamic of each element or independent neurons.

The main goal of this work is to develop a computational model of several pyramidal neurons of the CA1 hippocampal region, with diverse realistic morphologies, and the precise distribution of the main ion channels and synaptic inputs, for a future elaboration of the relevant elements of theta dynamics in CA1. A model of those characteristics, combined with the unique experimental access to extra- and intracellular recordings of the host laboratory, would certainly allow for novel insights on firing dynamics in deep and superficial pyramidal cells during the theta rhythm, and the role of the differential contribution of the excitatory and inhibitory synaptic inputs in both populations. For this reason, the work will not only attempt to properly model single cells, but also to build a code capable of integrating new properties, as new morphologies, more ion channels, more synaptic inputs, and more neuron types.

This main general goal can be divided into specific objectives:

- To learn how to use a specific software for neuronal dynamic simulation, such as NEURON [Hines and Carnevale], a simulating environment that allows the usage and development of new biophysical elements involved in modelling of realistic neurons.
- To implement a code that enable the automatic incorporation of any realistic morphology generated by reconstruction tools as NeuroLucida, using specific data bases as NeuroMorpho [Ascoli et al., 2007].
- To set the intrinsic properties of CA1 pyramidal cells, as reported by the literature.
- To set the main repertoire of ion channels of CA1 pyramidal cells, as reported by the literature.
- To set the main synaptic inputs of CA1 pyramidal cells, as reported by the literature.
- To simulate extracellular local field potential recordings, so that comparison with experimental recordings by the host laboratory are possible in the near future.
- To develop a basic cylinder of neurons, with an experimentally validated spatial distribution.
- To implement basic synaptic inputs that simulates the hippocampal theta rhythm.

1.2 Organization of this report

This work is divided into four chapters, followed by the conclusions:

- **Chapter 2: Physiological Foundations.** Our target is modelling pyramidal cells of the CA1 hippocampal region, so we first review hippocampal physiology with an emphasize on CA1 microcircuit elements by describing not only pyramidal cells, but also other critical neuronal populations such as GABAergic interneurons. We finally introduce concepts of the extracellular medium, its importance in the experimental environment, and how theta rhythm is seen extracellularly.
- **Chapter 3 : Theoretical and Computational Foundations.** Computational neuroscience has its roots back in 1952 in the hands of Hodgkin and Huxley, who made a mathematical model capable of reproducing the dynamics of an action potential in the giant squid axon. In this chapter we will explain this model formalism, and how it can be used to simulate a whole complex neuron. At the end, different approximations to compute the extracellular electric field are shown.

- **Chapter 4: Setting the settings.** This chapter comprises the main body of results regarding the basic model of CA1 pyramidal cell. The simulation software used and the neuron reconstruction tool are explained. Firstly, the code to flexibly import morphologies is described. Secondly, intrinsic properties are included and tested with current pulses.
- **Chapter 5: Synapses, connecting neurons.** After addition of the main synaptic inputs to CA1 pyramidal cells, the effect of some of the properties included in the previous chapter are seen in the EPSP, the excitatory post-synaptic potential.
- **Chapter 6: From the outside.** Finally, extracellular local field potentials are simulated on two simplified cases: single neurons, and a cylinder of neurons.

2

Physiological Foundations

Our target is modelling pyramidal cells of the CA1 hippocampal region, so we will first review the hippocampal physiology, with an emphasize on the CA1 elements, describing not only the pyramidal cells, but also the populations that affect them. We finally introduce the extracellular medium, its importance in the experimental environment, and extracellular functions of the theta rhythm.

2.1 The hippocampal formation

The hippocampal formation is a region of the brain involved in encoding of episodic (autobiographical events such times, places, associated emotions, and other contextual who/what/when/where/why knowledge, that can be explicitly stated), declarative (conscious, intentional recollection of factual information) and spatial memories. First evidence of this role came from studies of a patient, H. M., who after bilateral removal of the hippocampus in order to treat refractory epilepsy, was unable to form new memories in spite of retaining the old ones and being able to form new procedural memories (like learning how to play a new game) [Scoville and Milner, 1957]. Since then, a huge body of research aims to pursue for the underlying mechanisms.

2.1.1 Regions of the hippocampal formation

The hippocampus is a group of brain areas located in the temporal lobe, under the cerebral cortex, formed by the dentate gyrus (DG), the hippocampus proper, the subicular complex, and the entorhinal cortex (EC) [Andersen, 2007]. In general, the hippocampus receives inputs from all the sensory areas and projects to the prefrontal cortex, one of the cortical regions where long-term memories are believed to be stored and retrieved [Bird and Burgess, 2008]. The hippocampus proper, using the nomenclature proposed by Lorente de Nó in [Lorente de Nó, 1934], is divided into three parts: *Cornu Ammonis* 1, 2 and 3, or most commonly called CA3, CA2 and CA1 (figure 3.3). As the whole hippocampus is folded towards the inside of the skull, the nomenclature of some regions may appear contradictory: the *superficial* part of the dorsal CA1 is faced down, while the *deep* part is more external, opposite to the the brain cortex.

The CA3 region has recurrent connections within the CA3 subfield, and as a consequence, it is implicated in pattern completion and formation of associative memories in reciprocal interactions

with the dentate gyrus ([Hopfield, 1982], [Hasselmo et al., 1995], [Leutgeb et al., 2007]). CA3 projects its Schaffer collateral output onto CA1 and CA2 regions [Schaffer, 1892]. The CA2 is the least explored regions of the CA subfields because of its small size, but recently it has been shown that it has a specific role in forming social memories [Hitti and Siegelbaum, 2014]. A further description will be done in section 2.2.

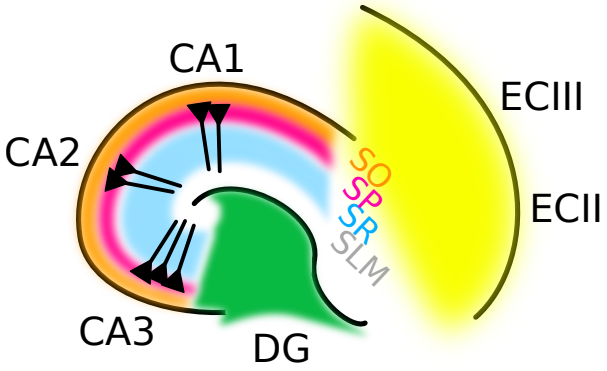

Figure 2.1: Hippocampal formation scheme

2.1.2 Layers of the hippocampus

There are four main layers in the hippocampus, from most superficial to deep: *stratum oriens* (SO), *stratum pyramidale* (SP), *stratum radiatum* (SR) and *stratum lacunosum moleculare* (SLM).

The principal layer that crosses the whole hippocampus (CA1, CA2 and CA3), known as *stratum pyramidale*, is formed mainly by the cell bodies of pyramidal cells (PC). Pyramidal cells were first discovered and studied by Ramón y Cajal. Pyramidal neurons are characterized by their distinct apical and basal dendritic trees and the pyramidal shape of their soma. The structure of pyramidal neurons, although stereotypical, is quite variable, both between regions (e.g. hippocampus vs. neocortex) and within regions (e.g. CA3 vs. CA1). Nevertheless, pyramidal neurons have a common morphology scheme: dendrites are separated into basal and apical boundaries. Several basal dendrites emerge from the base of the pyramidal soma. Each basal dendrite branches up to several times before terminating [Spruston, 2008]. There are dendritic domains with distinct synaptic inputs, excitability, modulation and plasticity which appear to be critical features allowing synapses throughout the dendritic tree to contribute to action-potential generation. These properties support a variety of coincidence-detection mechanisms, which are likely to be crucial for synaptic integration and plasticity [Spruston, 2008].

Above the *stratum pyramidale* we can find the *stratum oriens*, where basal dendrites are located, as well as another neuronal cell type, interneurons. GABAergic interneurons are characterized by their local connectivity so that their axons (and dendrites) remain limited to the region where the soma belongs. This feature distinguishes them from principal cells, which have axonal projections outside the brain area where their cell bodies are located [Freund and Buzsáki, 1998]. Principal cells as glutamatergic pyramidal cells are mostly excitatory, meaning that producing an action potential increases the probability of an action potential occurring in a postsynaptic cell. Interneurons release GABA, inhibiting their targets, via hyperpolarization (although, under some circumstances, they may also mediate depolarization or shunting). This will be discussed further in section 2.2.

The *stratum radiatum* is the layer next to the *stratum pyramidale*, where apical dendrites and some interneurons' somas are found. Finally, the most superficial layer, placed next to the SR, is the *stratum lacunosum moleculare*, where more distal dendrites are found.

In this work we will focus on the CA1 region, particularly on how afferents to the pyramidal cells determine their firing dynamics.

2.2 Pyramidal Cells of CA1

2.2.1 Excitation

CA1 is the main target of excitatory projections from many regions of the hippocampal formation:

(*i*) The Schaffer collaterals from CA3 are the main source of excitation onto CA1 pyramidal cells [Andersen, 2007].

$$\text{CA3} \rightarrow \text{CA1}\ (SR)$$

(*ii*) The ECII has two main excitatory neurons: pyramidal cells and stellate cells. Stellate cells project to dentate gyrus (DG) and CA3 [Varga et al., 2010, Ray et al., 2014]. Given their connection profile, the stellate cells of ECII are the main cell type responsible of collecting sensory information into the hippocampus. The DG projects to CA3 [Andersen, 2007]. As CA3 is the main excitatory source to CA1, both ECII and DG act indirectly on CA1.

$$\text{ECII} \rightarrow \text{DG} \rightarrow \text{CA3} \rightarrow \text{CA1}\ (SR)$$
$$\text{ECII} \rightarrow \text{CA3} \rightarrow \text{CA1}\ (SR)$$

It is noted that the ECII $\rightarrow$ DG connection is divergent, that is, over 10^5 stellate cells projects to 10^6 DG cells, one order of magnitude greater [Amaral et al., 1990]. Combining this with the fact that these last cells have a low firing frequency, it was suggested that the DG amplifies the differences over contextual information codified by EC, as in pattern separation circuits [O'Reilly and McClelland, 1994, Neunuebel and Knierim, 2014].

(*iii*) The PCs of entorhinal cortex layer III project to the *stratum lacunosum moleculare*, the most apical part of CA1 PCs [Andersen, 2007].

$$\text{ECIII} \rightarrow \text{CA1}\ (SLM)$$

2.2.2 Inhibition

Excitatory dynamics in the brain must be controlled by inhibition. It was in the hippocampus where the great diversity and specialisation achieved by GABAergic inhibitory neurons was first described [Freund and Buzsáki, 1998]. In this section the most relevant CA1 GABAergic populations are summarized:

(*i*) PV+ basket cells (PVbc): they inhibit the soma and the proximal apical dendrites of PCs [Kosaka et al., 1987]. PVbc are activated by CA3 PCs and by CA1 PCs [Valero et al., 2015].

$$\text{CA3} \rightarrow \text{PVbc} \dashv\!\rightarrow \text{CA1}\ (SP, SR)$$
$$\text{CA1} \rightarrow \text{PVbc} \dashv\!\rightarrow \text{CA1}\ (SP, SR)^*$$

* See equation (2.1) for further detail.

(*ii*) PV+ oriens-lacunosum-moleculare (O-LM): their dentritic arbour is located in the SO, mostly activated by CA1 PCs. They project to SLM, blocking the region where ECIII displays excitatory synapses. [McBain et al., 1994]

$$\text{CA1} \rightarrow \text{OLM} \dashrightarrow \text{CA1}\ (\textit{SLM})$$

(*iii*) CCK+ basket cells (CCKbc): as PVbc, they innervate the soma and proximal apical dendrites [Freund, 2003]. They are typically activated feedforward by Schaffer collaterals:

$$\text{CA3} \rightarrow \text{CCKbc} \dashrightarrow \text{CA1}\ (\textit{SP}, \textit{SR})^*$$

2.2.3 Deep and superficial pyramidal cells

At the end of the XIX century, Schaffer [Schaffer, 1892] thought of SP as the union of two layers: a superficial one, where cells were smaller and more compact, and a deeper one, where cells were bigger and scattered. Decades later, Lorente de Nó [Lorente de Nó, 1934] noticed that these cellular types presented distinct connectivities with both local interneurons and other regions. It wasn't until 2011 when, again, differences between deep (PC_{Deep}) and superficial pyramidal (PC_{Sup}) cells were examined. One seminal study lead by György Buzsaki [Mizuseki et al., 2011] found that superficial and deep PCs had different functionalities during theta rhythm. Recently, specific circuits for PC_{Deep} and PC_{Sup} within CA1 were additionally found:

(*i*) PVbc are mostly activated by PC_{Sup} [Lee et al., 2014].

$$\text{CA1 PC}_{\text{Sup}} \rightarrow \text{PVbc}$$

(*ii*) PVbc principally inhibit PC_{Deep} [Lee et al., 2014, Valero et al., 2015].

$$\text{PVbc} \dashrightarrow \text{CA1 PC}_{\text{Deep}}$$

Consequently, since CA3 → PVbc and CA1 PC_{Sup} → PVbc, when CA1 receives an input from CA3, PC_{Deep} activity is controlled by two different ways [Valero et al., 2015].

$$\begin{aligned} &\text{CA3} \rightarrow \text{CA1 PC}_{\text{Sup}} \rightarrow \text{PVbc} \dashrightarrow \text{CA1 PC}_{\text{Deep}} \\ &\text{CA3} \rightarrow \text{PVbc} \dashrightarrow \text{CA1 PC}_{\text{Deep}} \end{aligned} \tag{2.1}$$

(*iii*) CCKbc act mainly on PC_{Sup} [Valero et al., 2015].

$$\text{CCKbc} \dashrightarrow \text{CA1 PC}_{\text{Sup}}$$

(*iv*) ECIII sends more synapses to PC_{Deep} than to PC_{Sup} [Masurkar et al., 2017].

$$\text{ECIII} \rightarrow \text{CA1 PC}_{\text{Deep}}\ (\textit{SLM})$$

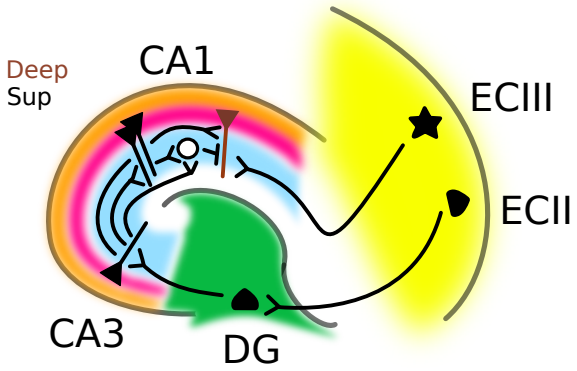

Figure 2.2: Hippocampal formation connectivity scheme

2.3 Electrophysiology in the hippocampus

2.3.1 Ion channels in the hippocampus

Until now we have been talking about «activation», «inhibition», «hyperpolarization »... without actually defining biophysically these terms. As we have seen in the previous section, the nervous system works in a electrochemical language, so the way to study and understand brain mechanisms is lead by technology sensitive to electric and/or chemical processes. At present, the prime methodology for studying neuronal circuit-connectivity and physiology under *in vitro* or *in vivo* conditions is electrical recordings with microelectrode arrays placed inside or outside neurons, so called intra- and extracellular recordings, respectively [Spira and Hai, 2013].

An action potential is a sudden rise and fall of the membrane potential, the electric potential of the intracellular medium with respect to the extracellular [Hodgkin and Huxley, 1952a]. The membrane potential is determined by differences on the ion concentrations between both sides of the membrane. The mechanism that allows the control of the membrane potential is the existence of specialised channels that are permeable only to some ions. The location and properties of ion channels therefore play essential roles in shaping electrical signalling in the neuron [Yuan and Chen, 2006].

In this section, we will review the most common ion channels found in CA1 pyramidal cells responsible for their firing dynamics [Hille, 2001].

Sodium channels

The fast activating voltage-gated Na^+ channels were one of the first quantitatively described ion channels by Hodgkin and Huxley in the squid giant axon [Hodgkin and Huxley, 1952a,b,c,d, Hodgkin et al., 1952] (see section 3.1 for more details). They are responsible for the depolarizing phase of action potentials, i.e., the fast increase of membrane potential at the beginning of the action potential. Sodium channels are encoded by 9 different genes [Yu and Catterall, 2003], and differences raising from different expression level of these genes lead to unique biophysical properties, such as half-maximal inactivation voltage, inactivation time constant and recovery time from inactivation, which, for example, controls the firing rate.

Apart from fast activating voltage-gated sodium channels, there are also persistent sodium channels. Given their persistent nature, they influence the spiking pattern and action potential waveform over longer periods.

Potassium channels

These channels tend to repolarize the membrane by conducting K^+ ions out of the cell. Leak channels are K^+ channels that have four transmembrane domains and contributes significantly to the resting membrane potential, around -65 mV, the relatively static membrane potential of cells (which is not an equilibrium potential as it relies on the constant expenditure of energy for its maintenance). The delayed rectifier potassium K_{DR} channels were first characterized as voltage-dependent (usually called voltage-gated, as we will see in section 3.1) by Hodgkin and Huxley [Hodgkin and Huxley, 1952a,b,c,d, Hodgkin et al., 1952], and are responsible for the repolarization phase of an action potential, i.e., the sudden decrease of the membrane potential (see 3.1 for more details). Depending on the molecular identity of these channels, they can differentially regulate firing rate and spike waveform in neurons.

Many types of K^+ channels are expressed in CA1 PCs. For example, there are some calcium-gated potassium channels like the big conductance (BK) channel that is both voltage- and

calcium- dependent, or the small conductance (SK) channel that is purely calcium-gated [Lancaster and Nicoll, 1987]. There is evidence that BK channels in CA1 pyramidal neurons inactivate during a train of action potentials. Given the elevation of intracellular Ca^{2+} during a single action potential and the concurrent depolarization activate BK channels [Lancaster and Adams, 1986], BK leads to broadening of action potentials and progressive reduction of fast after-hyperpolarization during the train [Shao et al., 1999]

Calcium channels

CA1 neurons express a multitude of calcium channels, each with their own distinct properties, that actively shape the action potentials. For instance, the L-type calcium channels gets activated at depolarized potentials, and are responsible for burst firing along with spike frequency accommodation [Magee and Johnston, 1995]; the T-type calcium channels get activated transiently at subthreshold voltage and can sustain intrinsic oscillations [Magee and Johnston, 1995].

HCN channels

The hyperpolarization-activated cyclic nucleotide-gated (HCN) cation non-specific channels, unlike most other channels, open on hyperpolarization of the membrane. It was found that these channels resemble channels belonging to the K^+ channel family but are also permeable to Na^+ ions, making these channels cation non-specific. In CA1 pyramidal neurons, its associated current, I_h, is expressed with an increasing density along the somatoapical axis [Magee, 1998]. These channels conduct a depolarizing inward current at a resting membrane potential, and affect their integrative properties at subthreshold voltages and the spike initiation dynamics [Magee, 1998, 1999].

2.3.2 The Local Field Potential

The electric current contributions from all active cellular processes within a volume of brain tissue superimpose at a given location in the extracellular medium and generate an electric potential [Buzsáki et al., 2012]. This summed electric voltage is known as local field potential, or LFP. Some of the processes from which the LFP arises are synaptic activity [Trevelyan, 2009], action potentials [Schomburg et al., 2012], and intrinsic currents [Llinás, 1988].

The electric field generated by differences of electric potential at two different points can be measured by extracellularly placed electrodes with submillisecond time resolution. In this way, the extracellular recordings allows simultaneous, cell-non-invasive, long term recordings of the extracellular field potential generated by the nearby neurons. Although it cannot capture directly subthreshold potentials generated by single cells, it implies an advantage over several other methods: the biophysics related to these measurements are well understood, what enables the development of reliable and quantitative mathematical models to elucidate how transmembrane currents give rise to the recorded electric potential. [Buzsáki et al., 2012]. On the other hand, intracellular recordings allow accessing to all electrophysiological repertoire of signals: subthreshold synaptic potentials, membrane potential, oscillations and action potentials. It has been shown that studying the temporal relation between the activity of single cells and the LFP has been a valuable tool to understand mechanisms of the brain [O'Keefe and Recce, 1993, Buzsáki, 2002].

2.3.3 Theta rhythm on the hippocampus

The layer structure of the hippocampal formation (one compact monolayer of principal cells) makes it perfect to study LFP dynamics [Schwartzkroin, 1975]. Moreover, given pyramidal cell's structure, excitation on the apical arbour generates an electric internal current towards the soma, which result in two separated and opposite current flows: to the inside of the cell in the apical dendrites, which from the outsize can be seen as a *sink*, and to the extracellular medium from the soma, seen as a *source*. Therefore, PC morphology allows these two flows to be enough separated to form an electric dipole, which will produce an electric field. This field can be measured by an extracellular electrode. This is why PCs contribute the most to extracellular electric field, in contrast to interneurons, which are shorter and spheric-shaped, so sinks and sources may overlap, reducing its extracellular contribution.

The characteristics of LFPs are modelled by the internal processes of nearby neurons, so any kind of synchronism in their activity would give rise to a strong electrical potential. In fact, if we place an electrode in the hippocampus, we will see an uninterrupted rhythmic oscillation. This oscillation is called *theta*, and consists of a rhythmic extracellular activity (4-12 Hz) that is considered the "on-line" state of the hippocampus [Buzsáki, 2002], and one of the most studied rhythms of the brain [Andersen, 2007]. Theta emerges during both locomotion and rapid-eyed-movement sleep (REM).

Different neuronal populations have a distinct firing preferred phase during theta oscillation, meaning that they have a rhythmic activity peak, out of phase with other types [Klausberger and Somogyi, 2008]: they are theta *modulated*. This time specification may be a key metric underlying all cortical operations [Klausberger and Somogyi, 2008]. We will now review the sequence of events on a theta cycle on CA1. For the sake of clarity, we will consider theta on the *stratum pyramidale* (note that, due to the electric dipoles formed by PCs, the extracellular phase changes across different layers, as sink and sources are separated), figure 2.3:

1. Ascending phase and theta peak: CCKbcs and PCs from ECIII fire in the ascending phase of theta and at the theta peak. Since ECIII projects to SLM, SLM shows a sink at this layer.

2. Descending phase: CA3 PCs are activated. Previously we mentioned that they project to the PVbcs, PC_{Sup} and PC_{Deep} . However, due to intrinsic properties of these cells, and to the $PC_{Sup} \rightarrow$ PVbc $\dashv\!\!\!\rightarrow PC_{Deep}$ circuit, they do not fire simultaneously at the decay phase: just after CA3 PC activation, PVbcs inhibite PC_{Sup} and PC_{Deep} before they can be activated. PVbcs, as most of the interneurons, not only have a higher spiking rate, but also are ready to fire [Klausberger et al., 2003].

3. Theta through: After the effect of the PVbcs' inhibition, PC_{Sup} fire, activating again the PVbcs which blocks PC_{Deep} . O-LM interneurons fire in the minimum of theta, although the underlying mechanisms are unknown. ECII is also activated in this phase.

4. Back to ascending phase and theta peak: at the same time as CCKbcs and ECIII, the PC_{Deep} are at last activated [Mizuseki et al., 2011]. We shall stress that apart from the absence of PVbcs blocking, the ECIII projection focused on PC_{Deep} implying an excitatory synapse's wave on the apical dendrites.

The reader may have found contradictory that, assuming that a slow delay between two connected neurons lasts around 5ms [Wayner and Emmers, 1958], firing along EC→DG→ CA3→CA1 takes about 80ms, instead of $(3 \times 5 =)$ 15ms. In order to understand theta cycle firing dynamics, and neuronal microcircuits in general, we must think of them in a more complex way that "receiving an excitatory synapse implies firing". Many interneurons (e.g., PVbcs and CCKbc)

act on the soma, or near apical dendrites [Klausberger and Somogyi, 2008], blocking potential activation due to excitatory flows from SLM. This is precisely what happens at the theta peak, and what remain as an uncomfortable paradox for years: the major PC population of CA1 do not fire when they receive their maximum depolarizing current flow from Schaffer collaterals [Kamondi et al., 1998, Buzsáki, 2002], which is exactly our question. Furthermore, the present technology's limits curtail the possibility to record dendritic activity, obscuring the underlying microcircuits. In this sense, biophysically realistic models will constitute a great advantage, since the intracellular information from all parts of the neuron could be available at every moment.

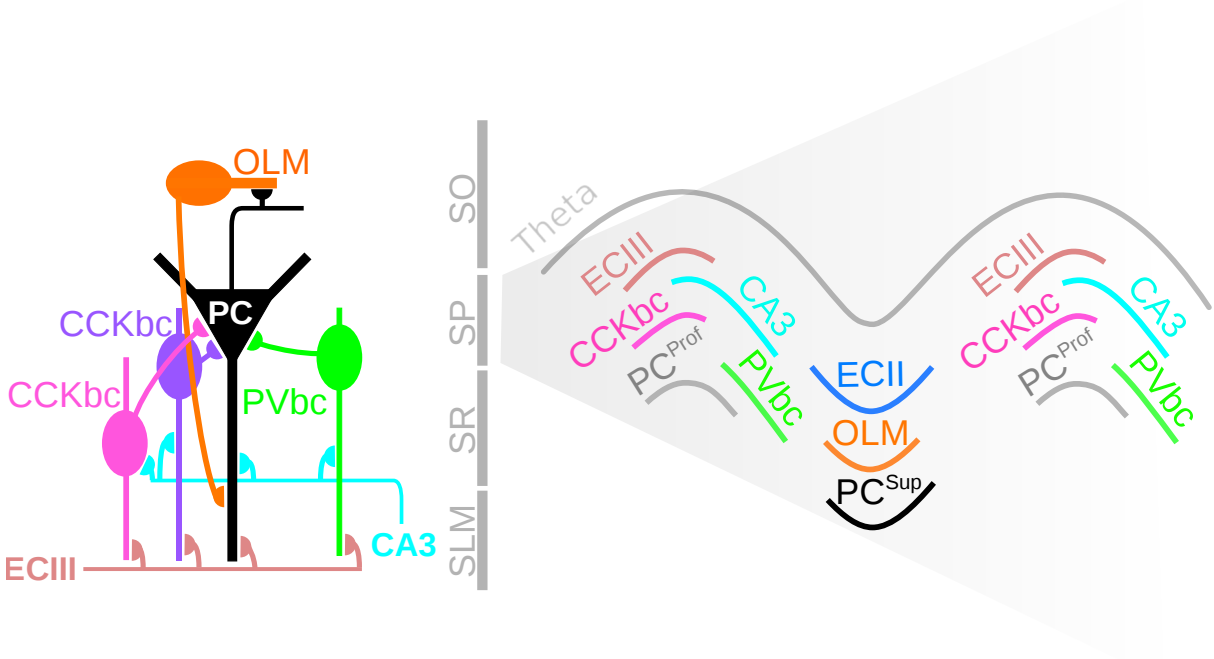

Figure 2.3: Theta modulation scheme. Each hippocampal population has a preferred theta phase to fire.

3

Theoretical and Computational Foundations

Computational neuroscience has its roots in 1952 in the hands of Hodgkin and Huxley, who made a mathematical model capable of reproduce the dynamics of an action potential in the giant squid axon. In this chapter we will expose and explain this model, and how it can be used to simulate a whole complex neuron. At the end, different approximations to compute the extracellular electric field are shown.

3.1 Hodgkin Huxley Model

Hodgkin and Huxley studied the origin of electrical excitability of the giant squid axon [Hodgkin and Huxley, 1952a,b,c,d, Hodgkin et al., 1952], and proposed a model which established that ions diffuse down their concentration gradient across neuronal membranes through transmembrane proteins which possess voltage sensitive gates. Hence the model was dubbed the gate model. Their assumptions were:

- Ion channel transitions *closed* $\Leftrightarrow$ *open* are conformational, and happen in response to changes in transmembrane voltage.
- The transition from one state to another is a first-order reaction. That means that the reaction depends on the concentration of only one reactant (an unimolecular reaction), or ion in this case.

Hodgkin and Huxley first developed an equivalent electric circuit model, shown in figure 3.1, and made the actual mathematical model by describing the dynamics of the electric current as an ordinary differential equations system of variables involved in the electrical circuit [Hodgkin and Huxley, 1952a]. They suggested that the current I could be carried through the membrane either by charging the membrane capacity, giving rise to the capacitive current, I_{C}, or by movement of ions through resistances in parallel with the capacity, the ionic currents, I_i (establishing that inward current would be positive):

$$I = I_{\mathrm{C}} + I_i = C_M \frac{dV}{dt} + I_i \tag{3.1}$$

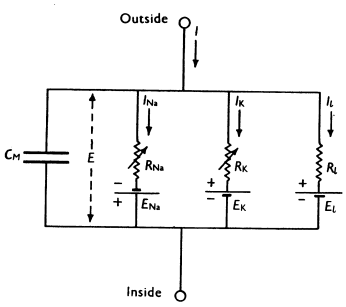

Figure 3.1: Hodgkin and Huxley's equivalent electrical circuit

where C_M is the membrane capacity per unit area (assumed constant). The membrane capacitance results from the fact that the membrane acts as a capacitor: the lipid bilayer is a thin insulator separating two electrolytic media, the intra- and extracellular spaces. The ionic current could be divided into several components carried by sodium and potassium ions, the I_{Na} and I_{K} currents, and the so called leakage current, I_l, made up by chloride and other ions:

$$I_i = I_{\mathrm{Na}} + I_K + I_l \tag{3.2}$$

Each component x of the ionic current is determined by a driving force (difference between the actual membrane potential V and an ion's equilibrium potential E_x) and a permeability coefficient, g_x, which has the dimensions of a conductance. Thus the ionic currents would be characterised as:

$$I_x = g_x(V - E_x) \qquad x \in \{\mathrm{Na}, \mathrm{K}\} \begin{cases} E_{\mathrm{Na}} \simeq 55 \text{ mV} \\ E_{\mathrm{K}} \simeq -90 \text{ mV} \\ E_l \simeq -55 \text{ mV} \end{cases} \tag{3.3}$$

Their experiments suggested that permeability of Na and K channels was influenced by the membrane potential: depolarization caused a transient increase in sodium conductance and a slower but maintained increase in potassium conductance; while repolarization of the membrane caused the opposite changes. Mathematically, it means that g_{Na} and g_{K} must be a function of both time and membrane potential:

$$g_x = g_x(V, t) \qquad x \in \{\mathrm{Na}, \mathrm{K}\} \tag{3.4}$$

In order to conceptually describe these time- and voltage-dependent increases and decreases, conductances were written in terms of *gating variables*, dimensionless variables that described the probability that a channel is open (so between 0 and 1):

$$g_{\mathrm{Na}} = \overline{g}_{\mathrm{Na}} m^3 h \qquad\qquad g_{\mathrm{K}} = \overline{g}_{\mathrm{K}} n^4 \tag{3.5}$$

where $\overline{g}_x$ is the maximal value of the conductance, m and h, the sodium channel activation, and sodium channel inactivation, respectively, and n, the potassium channel activation. The dynamics of these activation/inactivation probability variables was set as exponential decay ordinary differential equations, where the steady state values, $m_\infty, h_\infty, n_\infty$, and time constants, τ_m, τ_h, τ_n, depend on the membrane potential V:

$$\frac{dm}{dt} = \frac{m_\infty(V) - m}{\tau_m} \qquad \frac{dh}{dt} = \frac{h_\infty(V) - h}{\tau_h} \qquad \frac{dn}{dt} = \frac{n_\infty(V) - n}{\tau_n}$$

These equations were actually written in terms of α_y, β_y, rate constants for the ion channel y, related with the previous parameters as:

$$\alpha_y(V) = y_\infty(V)/\tau_y \tag{3.6}$$
$$\beta_y(V) = (1 - y_\infty(V))/\tau_y \tag{3.7}$$

giving rise to the final model of gating variables, equations 3.9, 3.12 and 3.15.

Collecting all these equations giving the total membrane current I as a function of time and

voltage, we finally have the Hodgkin and Huxley equation system:

$$I = C_M \frac{dV}{dt} + \overline{g}_{\mathrm{Na}} m^3 h (V - E_{\mathrm{Na}}) + \overline{g}_{\mathrm{K}} n^4 (V - E_{\mathrm{K}}) + \overline{g}_l (V - E_l) \tag{3.8}$$

$$\frac{dm}{dt} = \alpha_m (1 - m) - \beta_m m \tag{3.9}$$

$$\alpha_m = -0.1(V + 25)/(1 - \exp((V + 25)/10)) \tag{3.10}$$

$$\beta_m = 4 \exp(V/18) \tag{3.11}$$

$$\frac{dh}{dt} = \alpha_h (1 - h) - \beta_h h \tag{3.12}$$

$$\alpha_h = 0.07 \exp(V/20) \tag{3.13}$$

$$\beta_h = 1/(1 + \exp((V + 30)/10)) \tag{3.14}$$

$$\frac{dn}{dt} = \alpha_n (1 - n) - \beta_n n \tag{3.15}$$

$$\alpha_n = -0.01(V + 10)/(1 - \exp((V + 10)/10)) \tag{3.16}$$

$$\beta_n = 0.125 \exp(V/80) \tag{3.17}$$

3.2 Multi-compartmental Model

Attempting to model a whole neuron using Hodgkin and Huxley equations is an challenging task. To overcome these difficulties we must use some simplification that let us building a realistic model. Compartmental modelling is a very natural way of modelling dynamical systems that have certain inherent properties with conservation principles, as transmembrane dynamic has. A multi-compartment model is a type of mathematical model used for describing the way energies are transmitted among compartments of a system [Godfrey, 1983]. Mathematically speaking, this simplification reduces the state space of the system to a finite dimension [Agarwal and Lang, 2007].

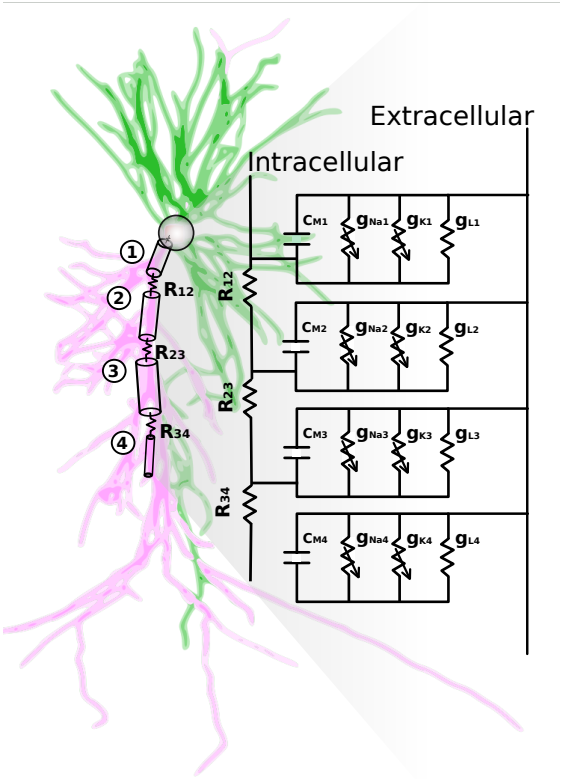

Figure 3.2: Multicompartmental model as the attainment of many Hodgkin and Huxley's equivalent electrical circuit.

This approximation states that each compartment is an equivalent entity. In our case, these equivalent entities would be the electric circuits modelled by Hodgkin and Huxley, discussed in the previous section, as shown in figure 3.1. Their positions and connections would determine the neuron morphology and dynamics. This strategy makes understanding of the electrical behaviour of complex neuron's morphologies easier and mathematically tractable. It is noted that the more compartments, the more realistic dynamics will emerge, but more computation power will be required.

As compartments are Hodgkin and Huxley's electric circuits, they are assumed to be isopotential and spatially uniform in its properties, i.e., $\overline{g}_{\mathrm{Na}}$, $\overline{g}_{\mathrm{K}}$, C_M, α_m, etc... are constant along

compartment. Membrane non-uniformity such as diameter changes, and voltage differences are defined in between compartments [Ermentrout and Terman, 2010]. Consecutive compartments are connected through resistances, allowing the current to pass along all the morphology.

3.3 LFP computation

Studies have shown that most of the extracellular space can be modelled as an isotropic volume conductor with no capacitive or inductive effects of the extracellular media at frequencies <3000Hz [Rall and Shepherd, 1968, Gold et al., 2006]. This allows the extracellular space to be modelled as a homogeneous purely ohmic conductor, so that the electric field, $\vec{E}$ (V/m), can be represented with a scalar extracellular potential, Φ (V) [López-Aguado et al., 2001, Anastassiou et al., 2010], as:

$$\vec{E} = -\nabla\Phi = -\left[\frac{\partial}{\partial x}\hat{x} + \frac{\partial}{\partial y}\hat{y} + \frac{\partial}{\partial z}\hat{z}\right]\Phi$$

where ∇ is the differential operator used to calculate the gradient of Φ, i.e., the 3D generalization of the derivative.

Both $\vec{E}$ and Φ can be derived from the electric current density I (A/cm^2) produced by the difference of ion concentrations between the inside and outside part of the cell membrane. In order to calculate I, we shall first determine the electric current density *flux*, J (molecules/s-cm^2). J arises from two processes: diffusion and electric drift. To get the diffusion flux, J_{diff}, we must apply Fick's law [Fick, 1855]:

$$J_{diff} = -D\frac{\partial[C]}{\partial x}$$

where D is the diffusion constant (cm^2/s), and $[C]$ concentration of the ion (molecules/cm^3) and x de transmembrane direction. The drift flux is caused by the electric field produced by the separation of charges, and it can be computed by the Ohm's law [Ohm, 1827]:

$$J_{drift} = \sigma_E\vec{E} = -\mu z[C]\frac{\partial V}{\partial x}$$

where σ_E electrical conductivity (molecules/V-s-cm), μ the mobility of the ion (cm^2/V-s), z the valence of the ion and $[C]$ the concentration. The net electrical flux is given by the Nernst-Planck approximation [Eisenberg, 2010]:

$$I = JzF = (J_{diff} + J_{drift})zF$$

where F is the Faraday's constant (96.480 C/mol). This is the so called passive flow of ions. It becomes zero when intracellular and extracellular ionic concentrations are equal, because it yields to a zero voltage. The equilibrium reversal potential of ion i, which is the transmembrane potential at which the membrane current carried by ion i is zeros, is:

$$E_i = \frac{RT}{zF}\log\frac{[C]_{out}}{[C]_{in}}$$

where R is the universal gas constant (8.314 J/K mol) and T is the temperature in Kelvin.

We can compute the extracellular electric potential having the electric current. However, given the complex morphology of the neurons, the computation of V from the real electric current distribution is intractable. Two main approximation are used: the point source approximation and the line source approximation.

3.3.1 Point source approximation

The approximation is to assume that the extracellular potential is generated by a *point* source in the centre of each neuronal compartment [Holt and Koch, 1999, Gold et al., 2006]. Given this, for n sources (i.e., compartments), the estimated field potential, Φ_{FP}, is computed as a linear sum of the potential due to each point source as:

$$\Phi_{FP} = \sum_{i=1}^{n} \frac{I_i}{4\pi\sigma r_i}$$

where I is the transmembrane current and r the distance from the point source.

3.3.2 Line Source Approximation (LSA)

In this approximation method, the extracellular potential generated from one compartment is computed from a continuous distribution of the transmembrane currents generated from a line that passes through the axis of the compartment [Gold et al., 2006]. Except from very close distances (less than 1μm away) from the recording location, LSA implementations are known to better approximate the extracellular signal and have been validated for hippocampal pyramidal neurons. For a single linear current source of length l, at a radial distance r from the recording site:

$$\Phi = \frac{1}{4\pi\sigma}\int_{-l}^{0} dx \frac{I}{l\sqrt{r^2+(h-x)^2}} = \frac{I}{4\pi\sigma l}\log\frac{\sqrt{h^2+r^2}-h}{\sqrt{s^2+s^2}-l}$$

$$\Phi_{FP} = \sum_{i=1}^{n} \frac{I_i}{4\pi\sigma l_i}\log\frac{\sqrt{h_i^2+r_i^2}-h_i}{\sqrt{s_i^2+r_i^2}-s_i} \tag{3.18}$$

where, being p point of the line that gives the shortest distance to the electrode, h is the shortest distance from p to the compartment and $s = l + h$ the largest distance from p to the end of the compartment.

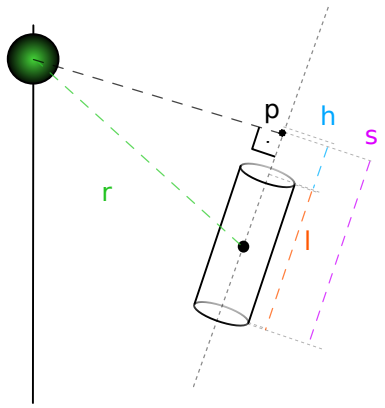

Figure 3.3: Measure scheme for LSA approximation

3.3.3 Current Source Density (CSD)

As we have just seen, the LFP is calculated from transmembrane currents, so it is natural to introduce the current source density (CSD), a scalar density field that characterizes each point

of space as a sum of the existent currents there:

$$C(\vec{r}) = \sum_j I_j \delta(\vec{r} - \vec{r}_j) \tag{3.19}$$

where $\delta(\vec{r})$ is the Dirac delta function. Current Source Density analysis is an extended method of analysis of extracellular electric potentials (LFP usually) recorded at multiple sites leading to estimates of current sources generating the measured potentials. [Jaeger and Jung, 2014]. It can be related with the extracellular potential:

$$V(\vec{r}) = \frac{1}{4\pi\sigma} \int d^3\vec{s} \frac{C(\vec{r})}{|\vec{r} - \vec{s}|}$$

where σ is the extracellular conductivity. Inverting this relation we can see that the CSD can be derived from the extracellular potential as:

$$C(\vec{r}) = -\sigma \Delta V \equiv= -\sigma \Delta \Phi_{FP} \tag{3.20}$$

where Δ is the laplacian operator. As the LFP is usually registered from multiarray electrodes, which we can think of them as a 1D line, CSD is usually simply computed as second derivative of the LFP. Using the finite differences approximation:

$$\begin{aligned} C(z) &= -\sigma \frac{d^2\Phi_{FP}}{dz^2} \simeq -\sigma \frac{\Phi_{FP}(z_{\text{El}} + \Delta z_{\text{El}}) - 2\Phi_{FP}(z_{\text{El}}) + \Phi_{FP}(z_{\text{El}} - \Delta z_{\text{El}})}{\Delta z_{\text{El}}^2} \\ C(\vec{r}) &\propto 2\Phi_{FP}(z_{\text{El}}) - \Phi_{FP}(z_{\text{El}} + \Delta z_{\text{El}}) - \Phi_{FP}(z_{\text{El}} - \Delta z_{\text{El}}) \end{aligned} \tag{3.21}$$

The resulted z-directed CSD is usually plotted along time, providing a useful and visual way to analyse the main dynamics of the neuron. This is the so called inverse problem on electrophysiology, where currents are computed from the Φ_{FP}.

4

Setting the settings

In this chapter, the main body of results regarding the basic model of CA1 pyramidal cell is shown. The simulation software used and the neuron reconstruction tool are explained. Firstly, the code to flexibly import morphologies is described. Secondly, intrinsic properties are included and tested with current pulses.

4.1 Simulation Software

The simulation environment used was NEURON [Hines and Carnevale, 2001, Hines and Carnevale]. NEURON is a simulation platform for modelling individual neurons and networks of neurons. It provides tools for conveniently building, managing, and using models in a way that is numerically sound and computationally efficient. It is particularly well-suited for problems that are closely linked to experimental data, especially those that involve cells with complex anatomical and biophysical properties; i.e., multicompartmental models. The languages used were, at first, Hoc, an interpreted language with C-like syntax, and finally Python, as it was recently adopted as an alternative interpreter. All Hoc variables, procedures, and functions can be accessed from Python, and vice-versa. This provided more degree of flexibility for setting up the anatomical and biophysical properties of models.

4.2 Morphology

A first step to start modeling is uploading neuron's morphology. As the aim of this work is to simulate a realist electrophysiological environment that can capture most features of the biophysical and morphological complexity of real neural networks we used realistic morphologies.

The database used was NeuroMorpho, a curated inventory of digitally reconstructed neurons associated with peer-reviewed publications, the largest collection of publicly accessible 3D neuronal reconstructions and associated metadata [Ascoli et al., 2007]. A number of neuron reconstruction tools especially software packages are available, such as Vaa3D [Peng et al., 2010], NeuronStudio [Rodriguez et al., 2008], or Neurolucida [Halavi et al., 2012, Aguiar et al., 2013], which perform detailed morphometric analysis of neurons, such as quantifying the number of dendrites, axons, spines, but also the length, width, and volume of dendrites, axons and soma. The procedure may be to either directly drawing neuronal processes in individual 2D sections of

a 3D image volume and manage to connect them, or using the 3D Virtual Finger which directly converts any 2D draw in a projection image to real 3D neuron processes [Peng et al., 2014].

The first reconstructed neuron, called I040913C2, was drawn by the host laboratory with Neurolucida, [Valero et al., 2015]. It is a CA1 rat pyramidal cell with classified dendrites, soma and axon. Another three CA1 PC morphologies from rat have been used: n409, n127, and n128, from Amaral's archive [Pyapali et al., 1998]. When results from these four morphologies are presented in this work, this colour code will be used.

As summarized in figure 4.1, this project flows from understanding the biological system principles by experiments and simulation to our final goal of generating testable hypotheses.

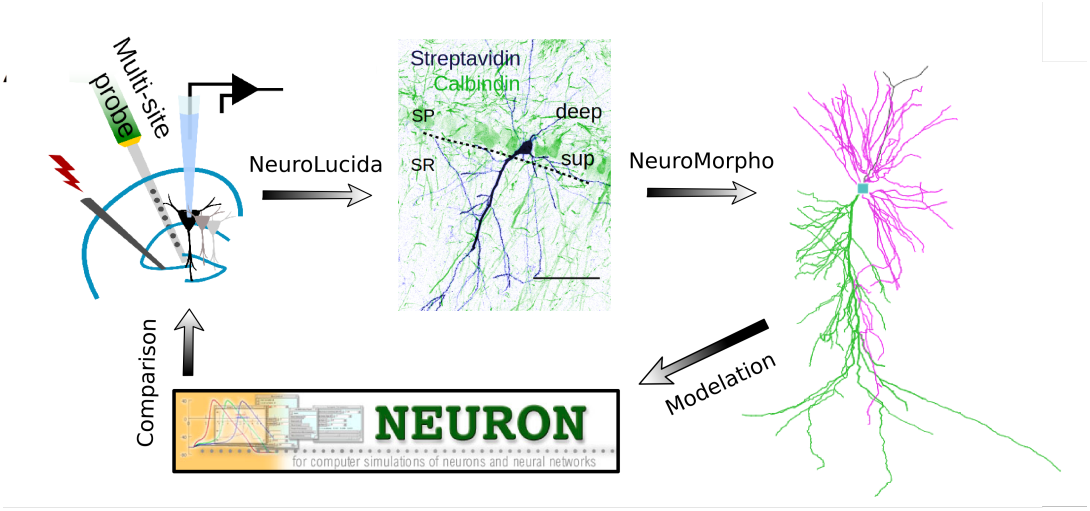

Figure 4.1: Schematic representation of the project

4.2.1 Importing neuronal morphology

Neurolucida saves the reconstructed data in a swc format, with the following scheme:

`Index Type X Y Z Diameter Parent`

where

- `Index` numbers the line, starting from `1`.
- `Type` is the part of the neuron the defined point belongs to: `1` for the soma, `2` for the axon, `3` for the basal dendrites and `4` for the apical dendrites.
- `X Y Z` are the 3D coordinates of the defined point.
- `Diameter` is the diameter of the defined point.
- `Parent` is the `Index` of the point to which the actual point should be connected.

When the `Parent`'s `Index` or the `Parent`'s `Type` does not coincide with the self `Index` or `Type` of the previous line, we can think of the next set of points as a new "morphological entity", different from the previous one. We will call these different "morphological entities" `Sections` (as NEURON command `h.Section()` suggests).

We can now understand the reasons for our selection of those four morphologies: 1) morphologies should be an almost complete reconstruction, with profuse dendrite arbours; 2) quality

of the swc file should be good enough (if the tracing is not done carefully and points are not placed in the appropriate order, the connections between sections may have no sense, nor neuronal morphology); and 3) there should be a whole and unique `Section` mapping the main apical dendrite.

Before importing neuronal morphology, we treated the swc files. First, points were rotated so the main apical dendrite was along the z axis. Then, contraction suffered by dehydration needed to reconstruct the neuron was corrected (perpendicular to the surface). NeuroMorpho also provides the average contraction factor, so points of the affected direction are divided by `(1-AverageContraction)`.

In order to organise swc data, four section lists were created, one for each section `Type`, called: `soma`, `axon`, `dend` (for basal dendrites) and `apic` (for apical dendrites). Each list contains as many `Sections` as there are in the swc file, according to the previous criterion (for clarity, the code will be written as simplified code):

```
def count_sections( typeSec ):
    # Counting how many sections of Type typeSec are there in the swc file
    num[typeSec] = sum([1 for i in Index if (Type[i] == typeSec)
                                        # The previous point is not its parent
                                    and ( (Parent[i] != i-1 )
                                        # Different type of its parent's
                                        or (Type[Parent[i]] != Type[i]) ) ])
    return num[typeSec]
```

Once created the different `Sections` , we can proceed to define the 3D points that will shape neurons, using `h.pt3dadd(x,y,z,diam)`. In order to avoid possible by default locations, it is convenient to clear the `Section` location with `h.pt3dclear()`. As `Sections` may be too large, with non uniform properties, it is convenient to divide them into more than one compartment, so we made as many compartments, or `Segments` in NEURON's terminology, as different points for each `Section` . A way to access to the properties of a particular `Segment` of a `Section` , say the x coordinate of the `Segment` i of the j apical dendrite is through the following command syntax `h.x3d(i,sec=apic[j])`. To finally set the topology of the neuron, connections between `Sections` are carried out with `ChildSection.connect( ParentSection )`.

The main apical dendrite for each neuron was then characterized: `apic[4]` for I040913C2, `apic[0]` for n409, `apic[0]` and `apic[1]` for n127 and `apic[0]` for n128, as it is shown in red in figure 4.2. In total, neurons modelled in this project have the following number of compartments: 4769 for I040913C2, 3449 for n409, 3244 for n127 and 3969 for n128.

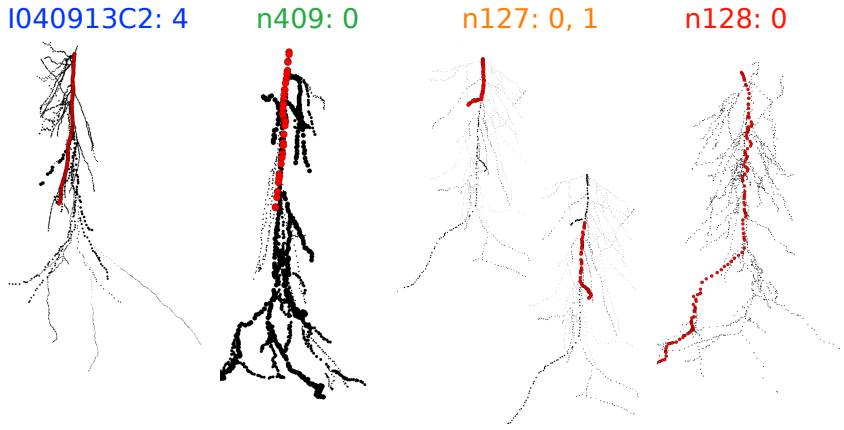

Figure 4.2: Main apical dendrite for each neuron

4.3 Passive properties

4.3.1 Setting passive channels

Passive channels

Initially, properties of passive channels were set following [Sinha and Narayanan, 2015]. The axial resistance (the force that impedes current flow through the axoplasm, parallel to the membrane), is uniform along the whole neuron, $R_a = 150\ \Omega\cdot\text{cm}$. The specific membrane capacitance C_M was set uniform at 1 $\mu\text{F/cm}^2$ for the somatic and axonal compartments, and at 1.8 $\mu\text{F/cm}^2$ for the rest of the neuron. The specific membrane resistivity, R_m varied along the main apical dendrite following a sigmoidal dependence on radial distance of the compartment from the soma:

$$R_m(z) = 80 + \left(\frac{0.4 - 80}{1 + \exp((225 - z)/30)}\right) k\Omega \cdot \text{cm}^2 \equiv \frac{1}{g_{\text{pas}}(z)} \tag{4.1}$$

For apical oblique dendrites, passive properties were similar across branches, by setting parameters according to parent compartments. The passive properties for basal dendrites and axonal compartments were the same as those for the somatic compartments.

It was found that if the contribution of dendritic spines to total surface area was not included in a multicompartmental model, the predicted input resistance values for CA1 PCs were several-fold larger than the experimental values [Srinivas et al., 2017]. Thus, a Spine-Scale factor (SS) was set as follows [Megías et al., 2001, Routh et al., 2009]:

Layer	**Diameter D (μm)**	**SpineScale**
SO	$\forall D$	2.51
SR	$1.6 \leq D$	1.69
	$0.55 \leq D < 1.6$	1.60
	$D < 0.55$	1.86
SLM	$0.35 \leq D$	2.10
	$D < 0.35$	1.71

Table 4.1: SpineScale factor depending on the layer and diameter of the compartment

To account for the extra surface area due to spines, in each dendritic segment R_m was divided by and C_M multiplied by the SpineScale factor:

$$R_m(z) \to \frac{R_m(z)}{SS(z, D)} \qquad\qquad C_M(z) \to C_M \cdot SS(z, D)$$

Figures 4.3 **a** and **b** show the final membrane capacitance C_M and passive conductance $g_{\text{pas}} = 1/R_m$ for the four morphologies included in this project. As can be seen, somatic membrane capacitance remains $1\mu\text{F/cm}^2$, as it is not affected by SS factor, whereas dendrites do show an increase, with basal branches exhibiting the larger SS effect. Passive conductances show the z-dependant sigmoidal function mentionned above (R_m is bigger the nearer to the soma).

HCN channels

Given their role in theta resonant properties of hippocampal neurons, HCN channels were also modelled. As they are not included in NEURON by default, its kinetic was directly programmed as part of this project. NEURON keeps track of the total current for each ionic species specified by the user and the effect of that current on the membrane potential. Management of these

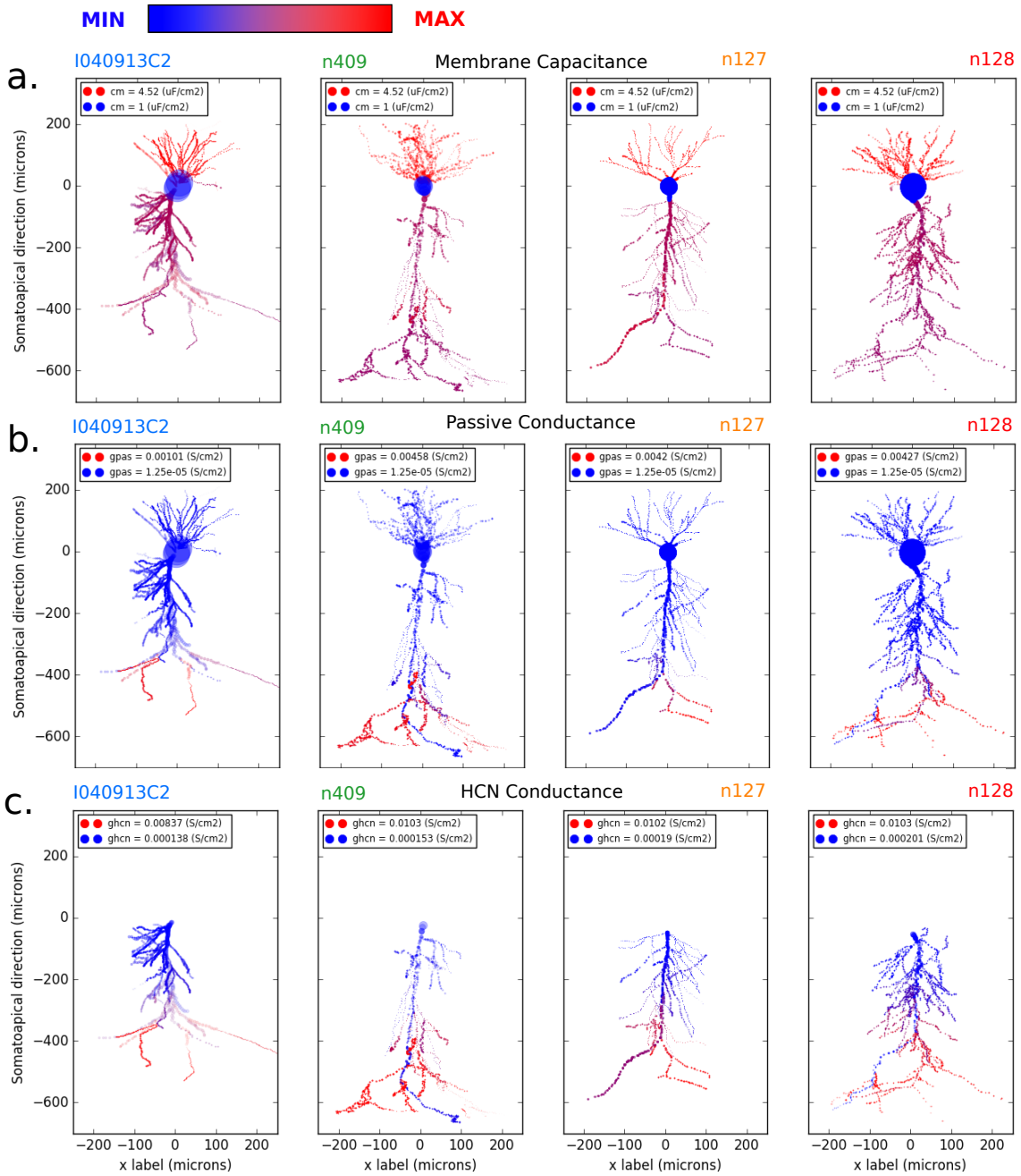

Figure 4.3: Display of the distribution of **a.** the membrane capacitance, **b.** the passive conductance and **c.** the HCN conductance, along all the neurons' morphologies. The neurons, from left to right, are I040913C3, n409, n127 and n128.

mechanisms (channels in which the model consists of current-voltage relationships and calculation of internal and external ion concentration changes) is lead by NMODL. ".mod" files, whose syntax closely resembles familiar mathematical and chemical notation, are passed to a translator that converts each statement into many statements in C, automatically generating code that handles details such as mass balance for each ionic species and producing code suitable for each of NEURON's integration methods [Carnevale and Hines, 2006].

The voltage dependence of the current through HCN channels, (I_h) was set as:

$$I_h = \overline{g}_h s(V,t) \cdot (V - E_h) \tag{4.2}$$

where $\overline{g}_h$ is the maximal HCN conductance, V the membrane potential and E_h the HCN-channel reversal potential, set at -30mV [Sinha and Narayanan, 2015]. $s(V,t)$ as the n, m, h variables of the Hodgkin and Huxley model, controls the voltage dependence kinetics of the HCN channel, obeying an exponential decay ordinary differential equation:

$$\frac{ds}{dt} = \frac{s_\infty(V) - s}{\tau_h} \tag{4.3}$$

where the steady state value, $s_\infty(V)$ and the time constant τ_h, depend on the voltage membrane as:

$$s_\infty(V) = \frac{1}{1 + \exp(V - V_{1/2})/8} \tag{4.4}$$

$$\tau_h(V) = \frac{F_\tau \exp(0.033(V + 75))}{0.013(1 + \exp(0.083(V + 75)))} \tag{4.5}$$

where F_τ represented a factor that was employed in scaling the (de)activation time constant of HCN channels without altering its voltage dependence, $F_\tau = 1$ by default, and $V_{1/2}$ denoted the half-maximal activation voltage of the HCN channel [Sinha and Narayanan, 2015], with:

$$V_{1/2} = \begin{cases} -82 \text{ mV} & \text{if } \Delta z \leq 100\mu\text{m} \\ 4 - 25\Delta z \text{ mV} & \text{if } 100 < \Delta z \leq 300\mu\text{m} \\ -90 \text{ mV} & \text{if } 300 < \Delta z\mu\text{m} \end{cases}$$

being Δz the z-distance to the soma, so that any apical oblique dendrite were kept the same as those in the parent main apical dendrite that it originated from.

The HCN-channel conductance was set with a sigmoidal gradient along the main apical dendrite [Sinha and Narayanan, 2015]:

$$\overline{g}_h(z) = 85 \left(1 + \frac{20}{1.0 + \exp((250 - z)/50)}\right) \ \mu\text{S/cm}^2 \tag{4.6}$$

and, as the $V_{1/2}$, its value was not kept as their apical dendrite parent. The g_{HCN} distribution along the apical arbour is showed in figure 4.3 **c.**.

4.3.2 Intrinsic passive properties

The first noteworthy effect of adding HCN channels is the abrupt change on resting membrane potential, V_{rest}, between 5 and 10 mV above the usual $V_{\text{rest}} \simeq -65$mV, which can be seen in figure 4.4 **a**. However, it must not seem odd, as the typical resting membrane potential of a cell arises from the separation of potassium ions from intracellular, relatively immobile anions across the membrane of the cell, and HCN channels are voltage-gated K^+ channels [Macri et al., 2012]. This rise is greater the further from the soma, which can imply a decrease in the driving force in the distant apical dendrites. The sudden fall observed in the resting membrane potential of neuron n127 due to the discontinuous apical trunk make the importance of a suitable main apical dendrite manifest. It takes around 200ms of the simulation's time to stabilize, as all compartments start at -65mV.

Current pulses were injected in the soma to characterize the neurons' response, with both depolarizing and hyperpolarizing currents ($I_{\text{ext}} = \{-0.3,\ -0.2,\ -0.1,\ 0.0,\ 0.1,\ 0.2,\ 0.3\}$ nA). Neuron responses are shown in figure 4.4 **b**. When the hyperpolarizing current is applied, some responses of the membrane potential show a depolarizing *sag*, that is, after reaching an initial minimum value, the voltage returns to a more depolarized steady-state value due to activation of I_h [Meena S et al., 2009]; by instance, cell n128's response to the -0.2 nA pulse.

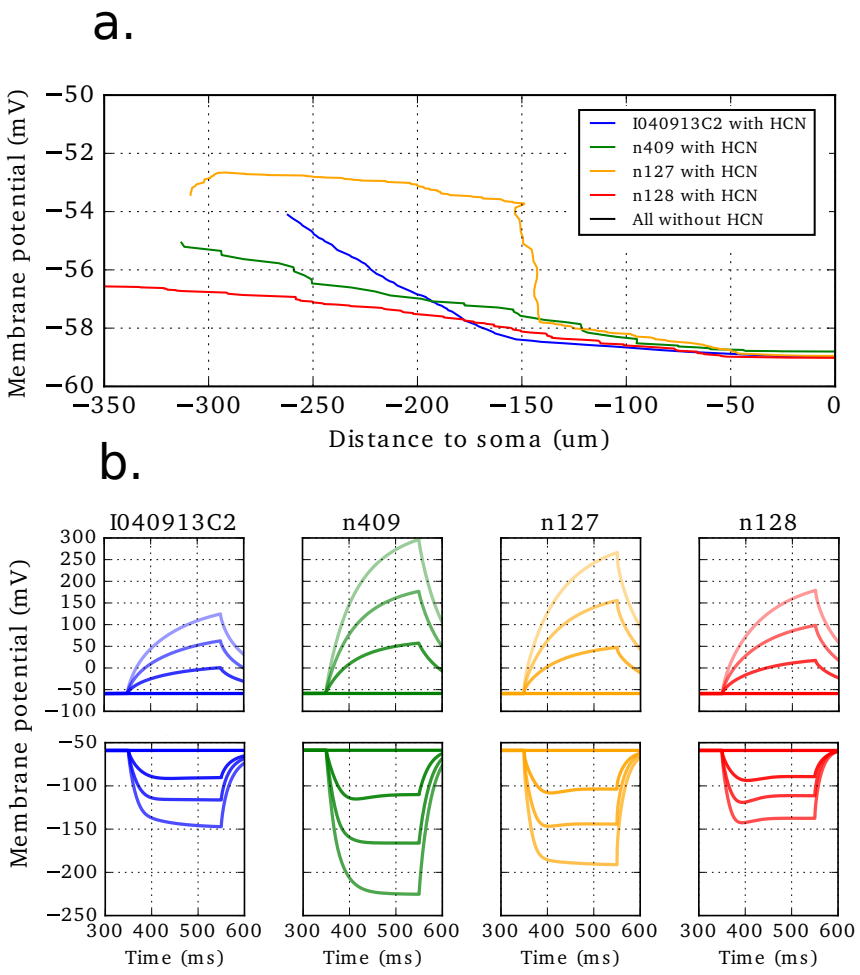

Figure 4.4: **a.** Membrane resting potential at different places of the main apical dendrite and the soma for all neurons, once inserted the HCN channels. **b.** Membrane potential in soma in response to both depolarizing and hyperpolarizing currents pulses, $I_{\text{ext}} = \{-0.3,\ -0.2,\ -0.1,\ 0.0,\ 0.1,\ 0.2,\ 0.3\}$ nA.

4.4 Intrinsic active properties

A major step in characterizing active properties of neurons is evaluating their input/output curve, i.e. to quantify the output of the neuron (firing rate) in response to an input range. Thus, $\{g_{\text{Na}}, g_{\text{K}}\}$ values will determine neuronal firing dynamics. For this reason, a parametric study was performed (figure 4.5). We chose to evaluate neuron I040913C2 with a fine-grained analysis, adopting a more coarse-grained evaluation for the other morphologies.

For each simulation, an 200ms current pulse of amplitude +0.1nA was injected into the soma, and neuronal response was evaluated as:

- did not fire at all (white circles).
- was continuously spiking, even before the application of the current pulse (red circles).
- fired just once after the pulse was applied (light blue circles).
- fired along the entire current pulse (dark blue circles).

As it can be seen in the figure, for the system to remain in a particular state either continuously spiking or spiking only during the current pulse, a linear dependence of g_{Na} and g_{K} must be

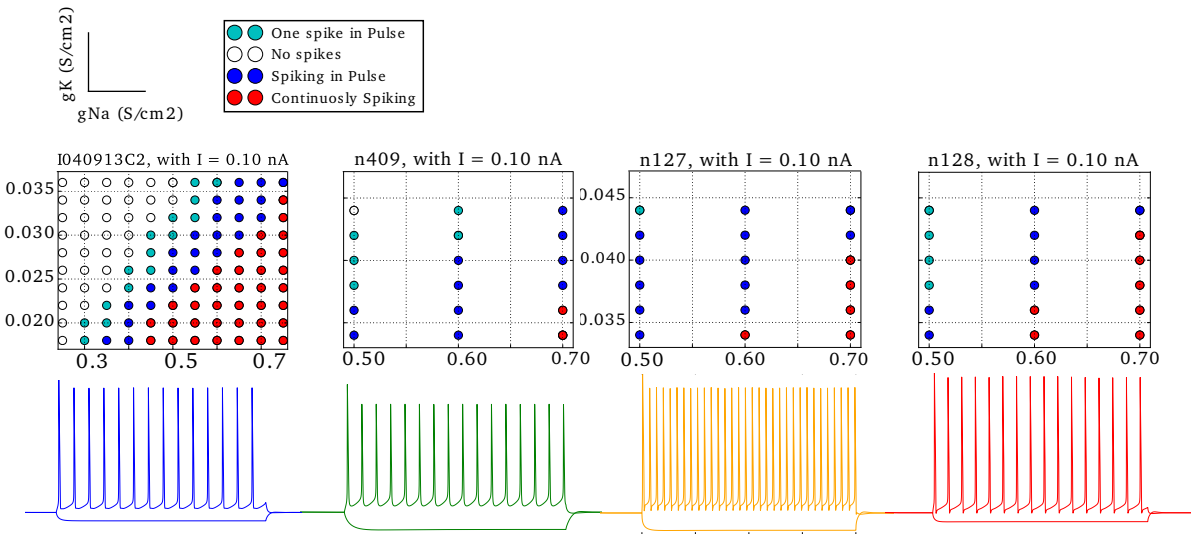

Figure 4.5: Parametric searching of $\{g_{\mathrm{Na}}, g_{\mathrm{K}}\}$ values.

satisfied. In other words, $g_{\mathrm{Na}}/g_{\mathrm{K}} \simeq \alpha$, a constant. In fact: if $g_{\mathrm{Na}}/g_{\mathrm{K}} \ll \alpha$, there is no sodium enough to counteract potassium flow, and depolarization can not be achieved; on the contrary, if $g_{\mathrm{Na}}/g_{\mathrm{K}} \gg \alpha$, the membrane potential does not need any external input to reach the threshold potential, so the cell fires continously. It was noted that when current was injected in this last case, firing rate was further increased. Out of the parametric region exposed in figure 4.5 and for $g_{\mathrm{Na}}/g_{\mathrm{K}} \gg \alpha$, membrane potential strongly depolarizes (up to -45mV) without firing.

Comparing the map of conductances we can observe that the $\{g_{\mathrm{Na}}, g_{\mathrm{K}}\}$ parameter landscape is different for each neuron, suggesting the critical role of neuronal morphology in firing dynamics.

	I040913C2	**n409**	**n127**	**n128**
g_{Na} (S/cm^2)	0.12	0.1	0.12	0.1
g_{K} (S/cm^2)	0.034	0.036	0.044	0.026

Table 4.2: Selected values for g_{Na} and g_{K} for each neuron.

Finally, the input/ouput intrinsic and I/V curves were estimated with conductance values displayed in table 4.2. The linear dependency of I/V curve, figure 4.6**b.** determines the input resistance of the neuron. We compared the simulated resistance for neuron I040913C3, $R_i \simeq 80$ MΩ, with that estimated experimentally, 30 MΩ, finding them in the same order of magnitude.

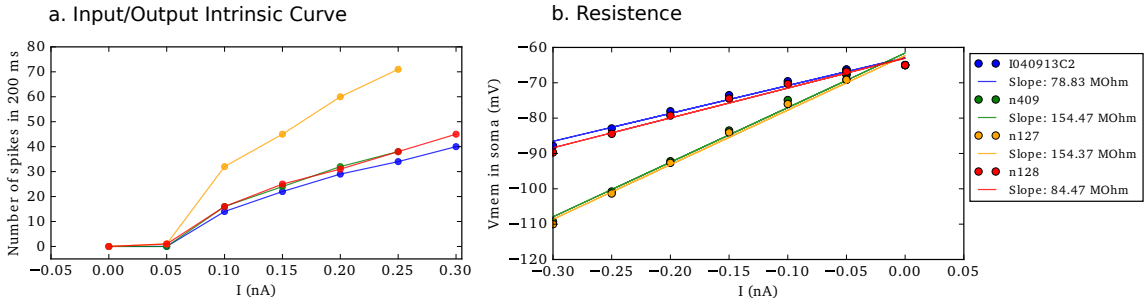

Figure 4.6: **a.** Input/Output intrinsic curve for each neuron. **b.** Intrinsic resistance calculation from I/V curves for each neuron.

5

Synapses: connecting neurons

Synapses are the main mechanism of communication between neurons, and hence a key element in achieving emergent dynamics of hippocampal microcircuits, as theta modulation. Chemical synapses are specialized ionic channels that respond to a ligand, so called neurotransmitter like GABA and glutamate. When the ligand binds to the synaptic receptor, the channel opens allowing ions to flow through, very similar to other active channels. In this chapter we will describe how synapses were modelled and integrated in the realistic simulation of CA1 pyramidal cells.

5.1 Synaptic inputs

5.1.1 Modelling the synapse

Synaptic current is conceptualized in a similar way as ionic currents of Hodgkin and Huxley model:

$$I_{\text{syn}} = g_{\text{syn}}(t)(V - E_{\text{syn}}) \tag{5.1}$$

where the conductance is time-dependent, and the E_{syn} determines whether it is an excitatory synapse ($E_{\text{syn}} = 0$ mV) or inhibitory (E_{syn}=-70). The dynamics of the synaptic conductance usually consist on a rising phase up to a maximal value, $\overline{g}_{\text{syn}}$, followed by an exponential decay. We have chosen the *Alpha Synapse*, which has the advantage to operate through a unique time constant, τ_{syn}, which we fixed at $\tau_{\text{syn}} = 1$ ms:

$$g(t)_{\text{syn}} = \overline{g}_{\text{syn}} \frac{t - t_{\text{onset}}}{\tau_{\text{syn}}} \exp\left(-\frac{t - t_{\text{onset}} - \tau_{\text{syn}}}{\tau_{\text{syn}}}\right) \tag{5.2}$$

NEURON allows building synapses without the presence of presynaptic signals. Instead, you can decide manually when and where the synapse is activated, setting t_{onset}. NEURON manages the synaptic current as a mechanism, which means that it calculates the internal and external concentration changes due to this current.

5.1.2 Excitatory Post-Synaptic Potential (EPSP)

Postsynaptic conductances cause changes of membrane potential being able to alter the firing probability of the postsynaptic cell. Thus post-synaptic potentials (PSPs) are called excitatory

(EPSPs) if they increase the likelihood of a postsynaptic action potential, or inhibitory (IPSPs) if they decrease this likelihood [Purves et al., 2001]. In this project, we will be dealing initially with excitatory synapses, so that synaptic changes on membrane potential will be reflected as EPSPs. In this section, in order to study and understand better the effect of synapses in neuronal dynamics, active properties are temporally removed.

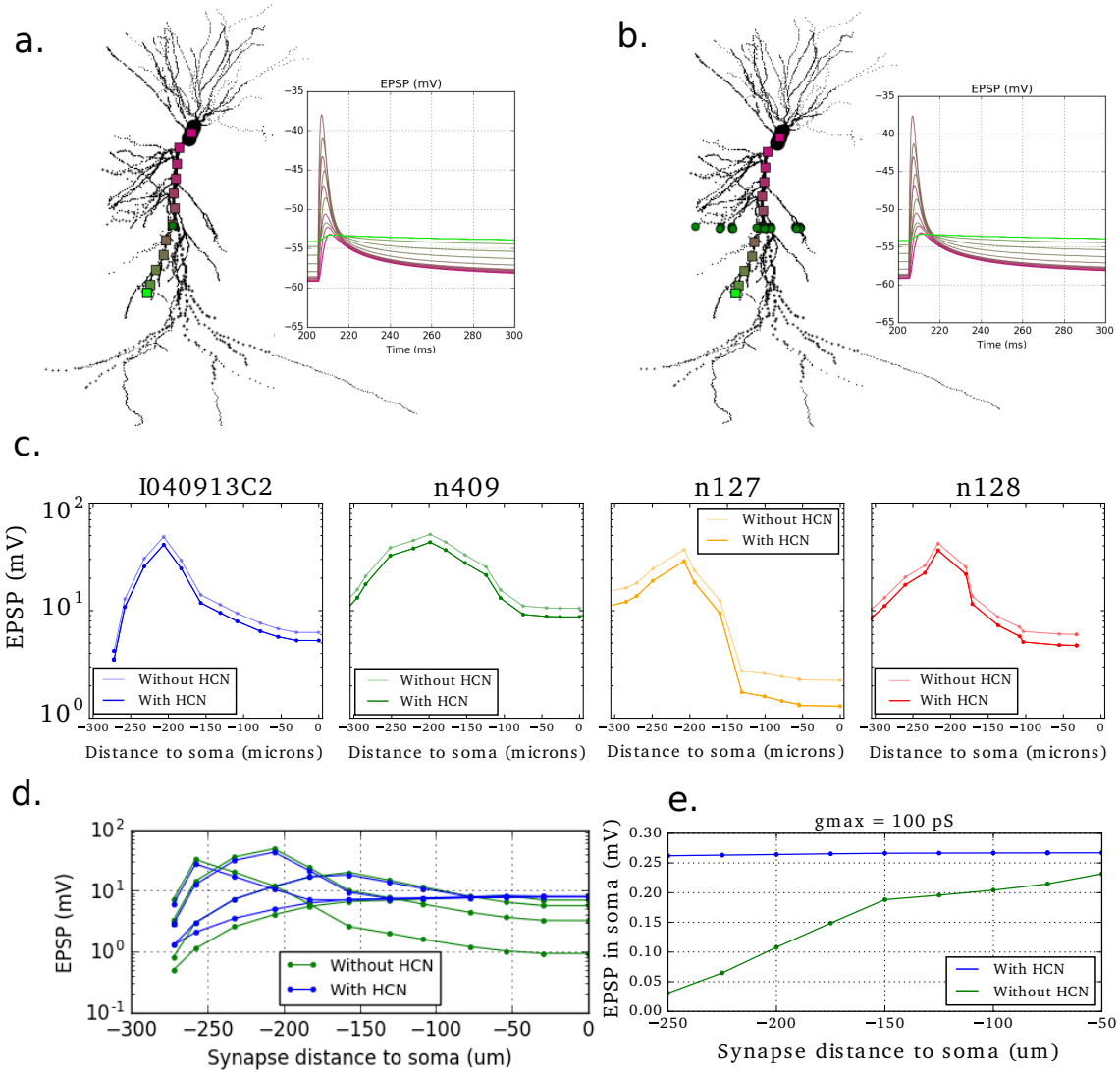

Figure 5.1: **a.** EPSPs along the main apical dendrite compartments after a single synapse activates at the main apical dendrite 200 ± 5 μm far from the soma. **b.** EPSPs along the main apical dendrite compartments after an array of synapses activate the apical dendrites 200 ± 5 μm far from the soma. **c.** Maximal EPSPs of the main apical dendrite compartments after a unique synapse setted on the main apical dendrite 200 ± 5 μm far from the soma for each neuron. **d.** EPSP along the main apical dendrite after a synapse pulse in positions $z = \{250, 200, 150, 50\}$ with and without HCN. **e** Independence of soma's maximal EPSPs with respect to the synapse's place

In the previous chapter, we mentioned the importance of having modelled a proper main apical dendrite. Figures 5.1 **a** and **b** reveal why: in figure 5.1**a** a single synapse is set in the main apical trunk, 200 ± 5 μm far from the soma, while in 5.1**b** all compartments at 200 ± 5 μm are receiving a synaptic input at the same time. As can be seen in this simulation, the influence of the apical trunk overrides any contribution of the secondary oblique dendrites. Since some recent

studies have been devoted to analyse the role of oblique dendrites in neuronal electrogenesis, we will not address this issue in this project.

Independently on the input configuration, both figures display the dynamics of the membrane potential of compartments from the main apical dendrite at different distances from the soma. Two main properties can be seen: first, there is a propagation delay from the synaptic site to the soma; second, the maximal EPSP attenuates with distance. This last fact is clearly shown in figure 5.1**c**, where the EPSP amplitude is plotted for each compartment along the main apical dendrite for each neuron (note that a semi-log plot is used). Particularly:

```
EPSPamplitude = max( V[i][idxwait:] ) - mode( V[i][idxwait:] )
```

where `V[i]` is the membrane potential of compartment `i`, and `idxwait = twait/dt` is the index of the time at which simulation started (in this case, `twait = 200 ms` as it is the time required for neurons to stabilize their resting membrane potential along the simulation).

5.1.3 Effect of HCN on the EPSP profile

In figure 5.1**c** it is represented the EPSP amplitude profile along the main apical trunk with and without HCN. Noteworthy, HCN channels attenuate EPSP amplitude [Sinha and Narayanan, 2015, Srinivas et al., 2017]. This can be related to the fact that resting potentials were depolarized by HCN: if the resting potential depolarize the driving force is smaller, leading to a similar EPSP absolute peaks, but different relative maximums. Another known effect of HCN channels was the independence of somatic EPSPs with respect to the synapse location: figure 5.1**d** shows the EPSP amplitude for different synaptic locations (single synapses at the main apical trunk), with and without HCN channels [Narayanan and Chattarji, 2010] in morphology 1040913C2, and figure 5.1**e** the EPSP amplitude at the soma for these configurations. In fact, it is the complex gradient distribution along the different compartments what ensures this effect [Sinha and Narayanan, 2015].

5.1.4 Effect of spines on the EPSP profile

We also confirmed the effect of spines on the EPSP profile along the main apical dendrite, as it has been seen that they attenuate EPSP amplitude near to the soma [Srinivas et al., 2017]. Figure 5.2 shows the comparison between the EPSPs with and without the SpineScale factor (both with HCN). As expected, as we approach the soma, the SpineScale factor diminishes the EPSP. Importantly, after accounting for spine scaling, the neuron input resistance get closer to the experimental values.

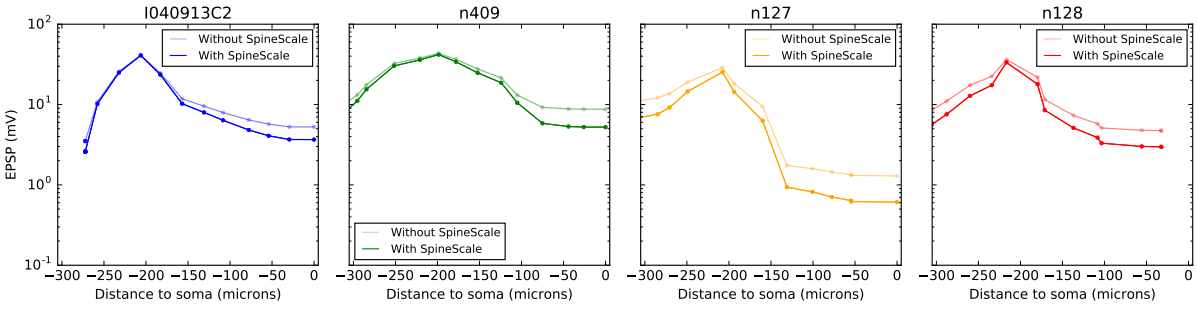

Figure 5.2: Attenuation of the EPSP the nearer to the soma due to the SpineScale factor.

5.1.5 Effect of dendritic diameter on EPSP

As the dendritically generated EPSP propagates passively down to the soma, it becomes exponentially smaller due to electrotonic cable properties. One important parameter to characterize this effect is the electrotonic length constant, λ_0, which is related to the squared root of the ratio between the membrane resistance and the axial resistance per unit length. Since the axial resistance $r_i = \rho_i/(\pi D^2/4)$, and membrane resistance, $r_m = R_m/\pi D$ depend both on the dendritic diameter D, the electrotonic length constant depends on D too [Rall, 1969, Holmes and Rall, 1992]:

$$\lambda_0 = \sqrt{\frac{R_m D}{4\rho_i}} \tag{5.3}$$

where ρ_i is the intracellular resistivity and R_m the membrane resistance. According to the cable theory, the fall of voltage along distance will obey the following formula:

$$V(x) = V_{\max} \cdot \exp(-x/\lambda_0) \tag{5.4}$$

Hence, the expected form of EPSP decay in a logarithmic scale is linear. However, Figure 5.2 suggest different attenuation dynamics instead. First, we considered whether this effect could be explained by current diffusion from secondary apical dendrites of smaller diameters using cell I040913C2. To this purpose, we compared the EPSP decay along the main apical dendrite with (figure 5.3 **a** orange) and without secondary dendrites (figure 5.3 **a** blue). As it can be seen, pruning branches makes poor effect on the EPSP profile, except for some amplitude reduction.

Next, we studied the effect of non-uniform diameter along the main apical trunk by equalizing the dendritic along distance to the soma for both previous simulations independently to the biggest and the smallest diameters. Figures 5.3 **b** and **c** shows the results from this experiment (note that the diameter of the soma is unchanged, so the sudden variation in the slope near $z = 0$ is caused by the big difference between those diameters). As it can be seen, when the dendritic diameter is similar along the apical trunk the EPSP decay obey a single exponential decay as predicted by cable theory. Thus, different attenuation dynamics result from non-uniform dendritic diameters. The biggest diameter presents a constant slope, which in fact coincides with the one near the soma.

5.2 Gaussian distribution of synapses in SR

As we previously mentioned, the main excitatory input to CA1 PC comes from the Schaffer collaterals of CA3 at the SR. Previous works characterized the number of the excitatory synaptic inputs in CA1 PCs. Particularly, it was seen that from the almost 17000 excitatory synapses received in the SR, 8871 were Schaffer inputs [Bezaire and Soltesz, 2013]. However, this quantity is larger than the number of compartments of the SR in our neurons.

At first, we considered having the numbers of synapses proportional to the total surface area of the neurons, assuming that a real neuron would have much more effective area due to its complex morphology and dendritic spines, so:

$$\begin{aligned} \text{My number of synapses} &= \texttt{My SR Area} \times \frac{\texttt{Known synapses in SR Area}}{\texttt{Known SR Area}} \\ &\simeq 10000\ \mu\text{m}^2 \times \frac{8871}{10000\ \mu\text{m}^2} \end{aligned}$$

where `Known synapses in SR Area` = 8871 as mentioned above [Bezaire and Soltesz, 2013] and `Known SR Area` = 1000 μm^2 [Routh et al., 2009]. We found that `My SR Area` = 1000 μm^2,

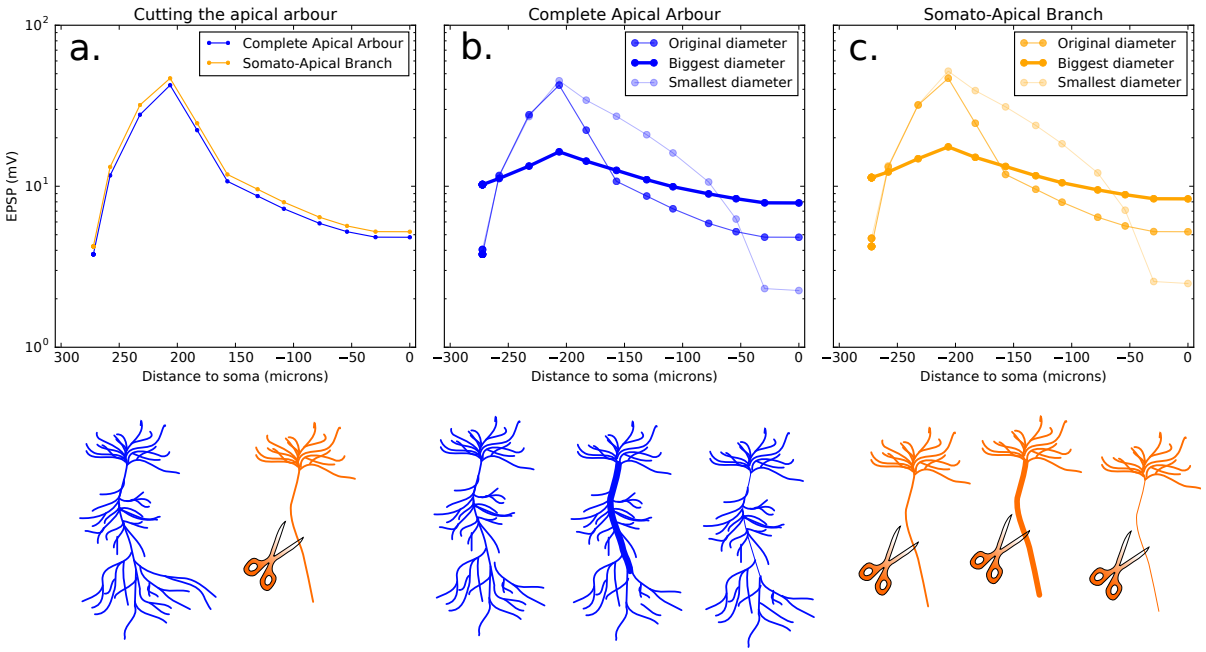

Figure 5.3: **a.** Comparison of the EPSP along the main apical dendrite with: the complete apical arbour (orange), a pruned apical arbour (blue) **b.** EPSPs with diameters of the main apical dendrite changed (complete dendritic arbour): thickest diameter (thickest line), thinnest diameter (thinnest line), and the original diameter **c.** EPSPs with diameters of the main apical dendrite changed (pruned apical arbour): thickest diameter (thickest line), thinnest diameter (thinnest line), and the original diameter

in agreement with literature. Thus, we considered the number of excitatory synapses to be 8871. We then chose a reduction factor $S_{\text{red}} = 10$ to make room for additional inhibitory or excitatory synapses to be implemented in future simulation steps. Hence the number of synapses chosen was $N_{\text{syn}} = 8871/S_{\text{red}} \simeq 800$. We set a Gaussian synaptic distribution with mean at 150 μm, and standard deviation of 50 μm. Figure 5.4 **a** shows the histogram of synaptic locations along the z axis in blue, and a black line representing the Gaussian distribution. The EPSP of the main apical dendrite after a simultaneously synaptic pulse with the Gaussian distribution, set at $t_{\text{onset}} = 205$ ms $=$ `twait` $+ 5$ ms, can be seen in figure 5.4 **b**.

5.2.1 Maximal synaptic conductance

Next, we chose the maximal synaptic conductance $\overline{g}_{\text{syn}}$ in equation 5.2. For figures 5.1, 5.2 and 5.3, a value of $\overline{g}_{\text{syn}} = 5000$ pS was used, so that the EPSP could be large enough to evaluate the electrotonic decay dynamics. When dealing with the Gaussian distribution a proper parametric study was performed by varying the maximal synaptic conductance from 10^{-1} pS to 10^{7} pS, as shown in figure 5.4 **c**. Here we calculated the amplitude of somatic EPSP from three cases: a single synapse at 50 μm and at 250 μm, and for the Gaussian distribution. As can be seen, the resulting curve is a sigmoid: if there is not enough synaptic current, the dendritically initiated EPSP can not reach the soma; for larger inputs the EPSP amplitude increases up to saturation at a given $\overline{g}_{\text{syn}}$. The conductance chosen was $\overline{g}_{\text{syn}} = 50$ pS to give somatic EPSP amplitudes of the order of few millivolts.

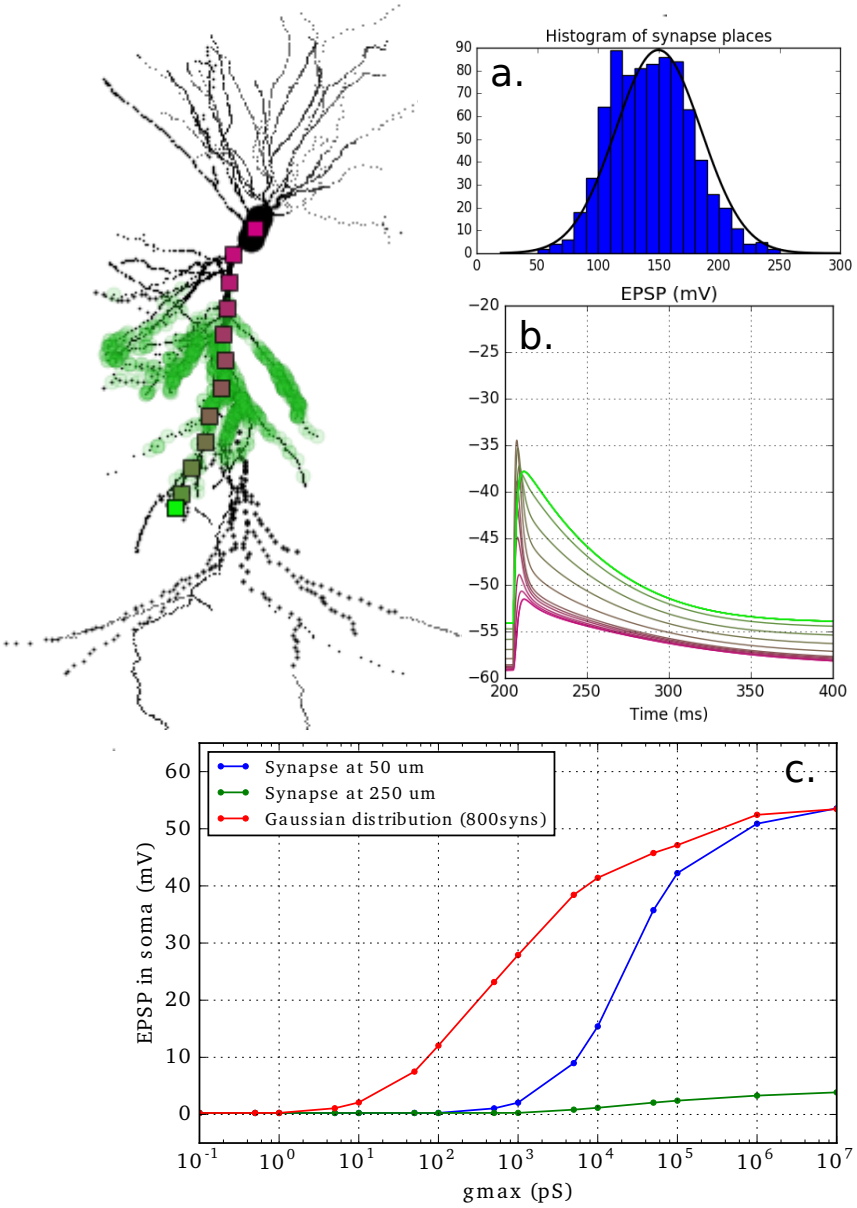

Figure 5.4: **a.** Excitatory synaptic distribution in SR. **b.** EPSP in the main apical dendrite after a synaptic pulse. **c.** Somatic EPSP depending on the maximal synaptic conductance for: a single synapse at 50 μm (blue), at 250 μm (green), a Gaussian synaptic distribution (red)

5.2.2 Maximal Na and K conductances re-parametrization

Once synapses were modelled, active properties could be reinserted. We observed that the previous values could not make the neurons respond adequately to synaptic inputs, i.e. they did not fire at all. Experimentaly, it has been shown that several-fold increases in channel density on the soma and on the axon initial segment (AIS) exert a critical functional role in firing electrogenesis [Lopez-Aguado et al., 2002]. Thus, we run a new parametric search by increasing active conductances in these compartments 5-fold with respect to dendrites (figure 5.5).

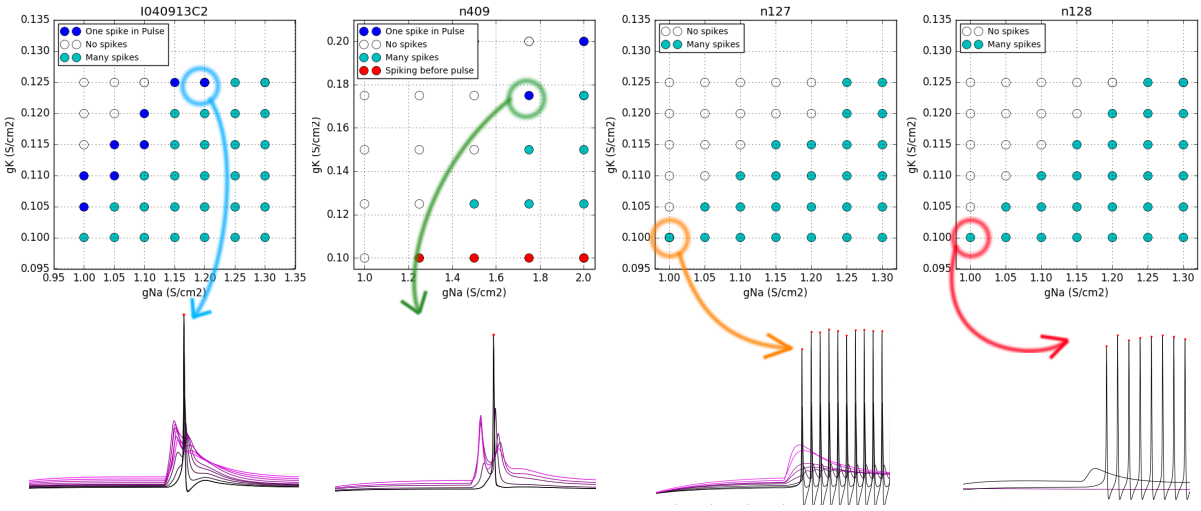

Figure 5.5: Parametric dependency of synaptic responses on AIS/somatic conductances. Bottom row show example cell responses; black, somatic membrane potential; dendritic responses are shown along a pink scale as we go further of the main apical trunk. Note how the spike starts in the soma, and propagates through the apical dendrite

6

From the outside

Most experimental recordings of hippocampal activity are extracellular, so called local field potentials (LFPs). Importantly, influencing theories of hippocampal function and its role in memory rely on studying hippocampal LFP oscillations during animals' behaviour. In this chapter, the extracellular environment is simulated by considering two simplified cases: LFP from single neurons, and LFP generated by a minimal cylinder of neurons.

6.1 Computing the LFP

The model used to compute LFP is known as line source approximation (LSA), where each compartment is thought as a line with an homogeneous current I_{mem} flowing into the extracellular medium. NEURON deals with the extracellular environment by the mechanism called `extracellular`. When you insert it to a `Section` , two layers of extracellular field are added [Hines and Carnevale]. It generates a total transmembrane current, `Imem`, equals to the sum of all the ionic currents through the membrane of each `Segment` , so that when there are no active properties, $I_{\text{mem}} = I_{\text{pas}} + I_{\text{cap}}$. Instead, when active and leaky currents are considered: $I_{\text{mem}} = I_{\text{pas}} + I_{\text{cap}} + I_{\text{Na}} + I_{\text{K}} + I_l$.

Before describing LFP calculations, we will talk about the way neurons were actually programmed, and how membrane potential values were stored, taking into account that at the end of this chapter more than one neuron will be managed. The way both neuron and membrane potential values were programmed were thought to be easily escalated.

6.1.1 Neuron class

A class was made, so multiple neuron objects could be instanced whenever required. As we have previously shown, each morphology needs different set of parameters. To compactly store those parameters, a python dictionary was created and saved with `pickle`, a module from python which implements a fundamental but powerful algorithm for serializing and de-serializing python object structures, as dictionaries [The Scipy community]. By instance, for neuron n409, the stored properties were:

```
Properties['n409'] = {}
```

```
Properties['n409']['gNa'] = 1.75
Properties['n409']['gK'] = 0.175
Properties['n409']['AISrel'] = 1/5.
Properties['n409']['ApicTrunk'] = [0]
```

Therefore, when a class is defined:

1. Both the neuron `Properties` and morphology `dataset` are imported, according to the declared `NeuronName` (the name of the morphology used), an attribute of the class.
2. Secondly, the lists of `Sections` are created from the .swc file. They have properties by-default (which in fact are the giant axon squid properties).
3. As `Sections` are objects, their properties can be modified by changing attributes. Attributes referred to positions, diameters and connections are all set next as stated in the .swc file. In order to allow for a particular distribution of cells in space, `X, Y, Z` variables are declared, and all points of the morphology are re-orientated. It is also possible to randomly rotate the whole neuron with `rot`:

$$\vec{r} \xrightarrow{\text{move}} \vec{r} + (\mathtt{X}, \mathtt{Y}, \mathtt{Z})$$

$$\vec{r} \xrightarrow{\text{rotate}} \begin{pmatrix} \cos(\mathtt{rot}) & -\sin(\mathtt{rot}) & 0 \\ \sin(\mathtt{rot}) & \cos(\mathtt{rot}) & 0 \\ 0 & 0 & 1 \end{pmatrix} \vec{r}$$

4. Biophysic properties are defined depending on what mechanisms you declare: `pas`, `extracellular`, `hcn`, or/and `hh`. The parameters are taken from `Properties`.
5. Finally, synapses are set. You can define whether their location (`syn_sec`, `zmin_sec`, `zmax_sec`), type (`syn_type_place` for a single synapse, an array or a gaussian distribution), how many there are (`syn_num`), and when are they activated (`syn_time`).

The simplified code of the constructor method shown below describes all these steps:

```
class Neuron_class( object ):
  # ------------------------------------------------------------------------
   # IMPORTING MORPHOLOGY AND PROPERTIES
   # ------------------------------------------------------------------------
   def __init__(self, NeuronName, numcell ):
     # Name of the morphology used
       self.NeuronName = NeuronName
       # Import morphology dataset
       self.dataset = pd.read_csv( self.NeuronName+'.swc' , delimiter = ' ',
              names = ['type','x','y','z','d','id_father'])
       # Import properties dictionary
       self.Properties = import Properties.pickle

       # ------------------------------------------------------------------------
       # SECTIONS
       # ------------------------------------------------------------------------
       # Number of section of each different types of section
       self.numsoma, self.numaxon, self.numdend, self.numapic =
           self.count_subsections( self.dataset )
       # We create three sections: somas, dendrites and apical dendrites
       self.soma = [ h.Section( 'soma', cell = self) for i in range(self.numsoma) ]
       self.axon = [ h.Section( 'axon', cell = self) for i in range(self.numaxon) ]
       self.dend = [ h.Section( 'dend', cell = self) for i in range(self.numdend) ]
       self.apic = [ h.Section( 'apic', cell = self) for i in range(self.numapic) ]
```

```
        # Sections corresponding to the main apical dendrite
        self.somatoapical = self.somatoapical_sections()

        # ------------------------------------------------------------------------
        # GEOMETRY AND TOPOLOGY
        # ------------------------------------------------------------------------
        # Position of the soma, different for each cell
        self.X, self.Y, self.Z = placecells[numcell]
        # Random self rotation
        self.rot = 360.*np.random.rand(1)
        # Making the morphology, moving and rotating the neuron according to X,Y,Z,rot
        self.basic_shape( self.X , self.Y , self.Z , self.rot , self.dataset )
        # Some basal dendrites of I040913C2 must be pruned
        if self.NeuronName == 'I040913C2': self.cut_basals()
        # Making the connections
        self.topol( self.shape3d )

        # ------------------------------------------------------------------------
        # BIOPHYSICS
        # ------------------------------------------------------------------------
        # We define what kind of channels we want in this class.
        self.mechanisms = ['pas', 'extracellular','hcn','hh']
        self.biophys( self.mechanisms )

        # ------------------------------------------------------------------------
        # EXCITATORY SYNAPSES
        # ------------------------------------------------------------------------
        self.syn_sec      = self.apic
        self.syn_zmin     = 50       # microns from soma
        self.syn_zmax     = 250      # microns from soma
        self.syn_type_place = 2      # {0: point}, {1: line}, {2: gaussian}
        self.syn_num      = 800      # Number of places containing synapses
        self.syn_time     = twait + 2
        self.set_synapse()
```

As the model is meant to be escalated, all instanced cells are stored in a list. For 5 neurons with the I0409132 morphology, the list `cells` would be instanciated as:

```
NumberOfCells = 5
cells = [ Neuron_class("I040913C2",numcell) for numcell in range(NumberOfCells) ]
```

6.1.2 `Recordings` dictionary

NEURON has its own vector class `Vector` which provides functions for manipulating one-dimensional arrays of numbers. We can save the value of the variables as `Imem` or `Vmem` along simulation time through the `Vector`'s method `record`. For instance, to record the I_{Na} at the beginning of the first apical dendrite you would need to:

1. Instance the `Vector`: `Ina = h.Vector()`, where the `h` is the Hoc module for python.
2. Calling the recording method. It requires to specify the position of the compartment and the variable to record:
   - The position of the compartment needs to have the following form: `Section(Location)`, where `Location` is a number between 0 and 1, 0 if the `Segment` is at the beginning of the compartment, 1 if it is at the end.

- As NEURON is prepared to incorporate any new self-defined method, as our HCN channels, the variable to be recorded should be called using `_ref`, followed by the name defined in the NMOD files, followed by the name of the mechanism.

leading to: `Ina.record( apic[0](0)._ref_ina_hh)`.

In this case, `Ina` would be a pointer. We can convert the information addressed by this pointer into a python array through `Ina.to_python()`.

In order to organize the records, a python dictionary `recordings` was made:

1. The keys of the dictionary are elements of the list of neurons, `cells`.
2. The recordings of the neuron i of the list would be accessed by

   `recordings["cell%d"%i]`

   which is also a dictionary, whose keys are the `Sections` .
3. The recordings of the jth apical `Section` of neuron i would be accessed by

   `recordings["cell%d"%i]["apic%d"%j]`

   which is also a dictionary, whose keys are the `Segments` .
4. The recordings of the variable x of the kth compartment of the jth apical `Section` of neuron i would be accessed by

   `recordings["cell%d"%i]["apic%d"%j][k]["x"]`

   which finally are the NEURON vectors.

The simplified code of the setting of the recordings is shown below:

```
def set_recording( cells ):
    recordings = {}
    CellNumber = 0
    # In each cell:
    for cell in cells:
        CellName = "cell%d"%CellNumber
        recordings[CellName] = {}
        # Each section of the cell:
        for Section in cell.soma+cell.dend+cell.apic+cell.axon:
            # Name of the section
            SecName = "%s%d"%(SectionType,SectionNumber)
            recordings[CellName][SecName] = {}
            # In each segment of each section:
            NumberOfSegments = Section.nseg
            for Seg in range(NumberOfSegments):
                # Location: position of the compartment: 0 begenning, 1 end
                Loc = Seg/NumberOfSegments
                recordings[CellName][SecName][Seg] = {}
                # Instanciate NEURON's vectors
                recordings[CellName][SecName][Seg]['Vmem'] = h.Vector()
                recordings[CellName][SecName][Seg]['Imem'] = h.Vector()
                # Setting the variable and place to record
                recordings[CellName][SecName][Seg]['Vmem'].record(
                        Section(Loc)._ref_v )
                recordings[CellName][SecName][Seg]['Imem'].record(
                        Section(Loc)._ref_i_membrane )
                # Saving the position
```

```
                recordings[CellName][SecName][Seg]['pos'] = [
                        h.x3d(Seg,sec=Section),
                        h.y3d(Seg,sec=Section) ,
                        h.z3d(Seg,sec=Section),
                        h.diam3d(Seg,sec=Section) ]
        CellNumber +=1

    return recordings
```

By this way, you can easily move and asses different desired variables for each compartment of each cell.

6.1.3 Computing the LFP from the `recordings` dictionary

The `recordings` dictionary makes the computation of LFP signal simple: it is looped over cells, over `Sections` and over `Segments` , and for each `Segment` the position of its extremes and `Imem` is obtained. Calling `a` and `b` the extreme positions, the elements of the LSA approximation would be:

- Position of the Electrode: $\vec{r}_{\text{El}} = (x_{\text{El}}, y_{\text{El}}, z_{\text{El}})$. x_{El} and y_{El} are kept fixed, and different electrodes are at different z_{El}.
- Line through the compartment: $\vec{p}(t) = \vec{a} + t \cdot (\vec{b} - \vec{a})$. We need t_0 such that a minimum distance between the line and the electrode is achieved:

$$t_0 = \frac{(x_b - x_a)(y_a - y_{\text{El}}) - (x_a - x_{\text{El}})(y_b - y_a)}{|\vec{a} - \vec{b}|^2}$$

- The minimum (`h`) and maximum (`s`) distances from $p(t_0)$, and compartment length (`l`) are calculated as:

$$\texttt{h} = \texttt{min}(|\vec{p}(t_0) - \vec{a}|, |\vec{p}(t_0) - \vec{b}|)$$
$$\texttt{s} = \texttt{max}(|\vec{p}(t_0) - \vec{a}|, |\vec{p}(t_0) - \vec{b}|)$$

Then, the LSA equation (3.18) of Chapter 3, is applied, with an extracellular resistivity of $\rho = 3.33$ Ω·m [Sinha and Narayanan, 2015].

Results are shown in figure 6.1 for two different morphologies. For both I040913C2 and n409, LFP signals are calculated for 800 simultaneous synapses (supra-threshold response) and for half those synapses (sub-threshold response). One useful experimental calculation is obtaining current-source-density (CSD) signals as the second spatial derivative of laminar LFP recordings. Thus, we also simulated the CSD signal from 100 micron separation LFP, which is plotted after spline interpolation. Current sinks and sources are abstract concepts that define regions from which synaptic currents flow through neuronal membrane. For instance, when positive charges flow across the membrane to inside the cell (sink) this creates a transient negativity; conversely, when negative changes enter the cell a transient positivity is detected (source). Note that sink and sources may reflect both active (i.e. synaptic) or passive currents (i.e. return currents). CSD sinks are represented in blue and, in this case, they indicate the activation of synaptic inputs at SR: this activation depolarizes membrane potential so a recruiting of positive ions is needed, leading to a ion flow to the *inside*. The other sinks detected at the SO and SLM strata reflect passive return currents flowing through these compartments. Sources are represented in red, and they are mainly present near the soma where the recruited cations are released to

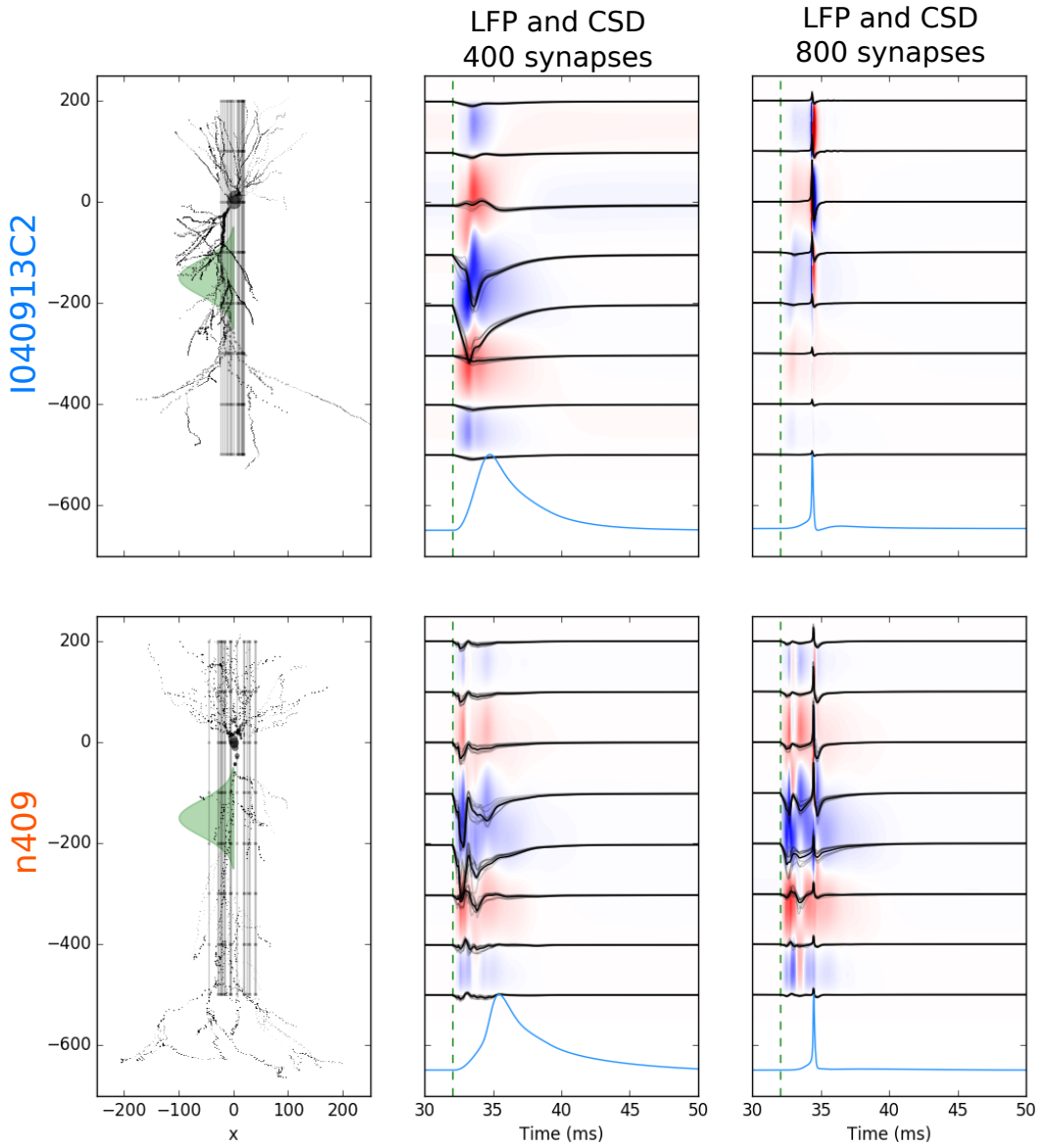

Figure 6.1: LFP and CSD after a synaptic input of 400 synapses (middle) and 800 synapses (right). For LFP, 10 different $(x_{\mathrm{El}}, y_{\mathrm{El}})$ were randomly chosen (whose LFPs can be seen in light black), and the LFP mean was plotted in dark black. The CSD is plotted behind the LFP, sinks represented in blue, sources represented in red. At the bottom, the somatic membrane potential is shown.

the extracellular medium, leading to an apparent positive flow to the *outside*. In light blue at bottom, the somatic membrane potential is shown.

By definition, dependence of LFP on neuronal morphology is notorious. Note that exactly similar synaptic inputs at exactly same locations (plotted as a green Gaussian at left) and timing (green dashed line), resulted in different LFP profiles in the two neuronal morphologies. Moreover, LFPs also depend on electrode location. This is typically exploited experimentally to infer the position of the electrode along the different hippocampal strata or with respect to a single-cell being recorded extracellularly. To limit this effect, 10 different $(x_{\mathrm{El}}, y_{\mathrm{El}})$ were randomly chosen (whose LFPs can be seen in light black):

```
AngleElectrode  = 2*pi*rand
```

```
RadiusElectrode = minDistance + maxDistance*rand
```

where `minDistance`= 5 μm, and `maxDistance` = 50. The mean of those LFPs was plotted in dark.

There are some elements of the simulated LFP that are also present in experimental records:

- The downwards shape of the field EPSP at SR ($z_{\mathrm{El}} = -200$ μm) with 400 synaptic inputs for both morphologies.
- Phase reversal of LFP from SR ($z_{\mathrm{El}} = -200$ μm) to SP ($z_{\mathrm{El}} = 0$ μm) more clearly seen in cell I040913C2 when it does not fire: while there is a sink in the SR, there is a source in SP.

However, individual morphological features contribute strongly to the LFP form, and the whole simulated LFP profile along the main apical axis is not yet as realistic. For our model to reproduce the experimental results, more neurons may be required.

6.2 Making a cylinder of neurons

6.2.1 Building the cylinder

The way the `Neuron_class` was programmed makes possible to easily build an environment of many neurons. In addition, PCs in CA1 region are poorly connected each other, so it is possible to build a many-CA1 PCs-system without including synaptic connections between the different neurons. This means that to have `numcells` neurons in our model, we just have to instantiate `numcells` neuron objects. A first step though is to determine the tri-dimensional layout.

We considered a basic module of a number of neurons in a cylinder for some obvious reasons: 1) there is a clear axis in space, the main apical trunk, so that there must be a preferred direction for the intracellular current flow (z); 2) the contribution on the electric potential Φ_{FP} of the current of a particular compartment depends on the *module* of the distance $\Phi_{FP} = \Phi_{FP}(|\vec{r}|)$, not the direction, so any other preferred axis should not be induced. The cylinder meets these two requirements. In order to satisfy the second condition, an homogeneous distribution on $\{x, y\}$ should be imposed. We proceed to make a spiral that changed its angular increment as the radius grew [Ibarz et al., 2010]:

```
Radius_Initial = 20.
Angle = 0
Separation = 30
Radius = Radius_Initial
for cell in range(numcells):
    # Spiral
    x = Radius * cos( pi*Angle/180 )
    y = Radius * sin( pi*Angle/180 )
    IncrementAngle = ( 180*Separation )/( pi*Radius )
    Angle += IncrementAngle
    Radius = Radius_Initial + Radius_Initial*Angle/360
```

The final distribution is displayed in figure 6.2 **a** for a total of 20 neurons with either the two neuronal morphologies used. The (z) distribution of neuron's somas within the SP layer followed experimental data from the host laboratory, figure 6.2 **c**. The numpy module of python allows generating random samples given a 1D array: from the histogram of the experimental positions

of the CA1 pyramidal somas two arrays were obtained: `placesModel` and `numCellsModel`. Given these two arrays, the different height of the neurons was chosen by:

```
z = np.random.choice( placesModel, p = numCellsModel/sum(numCellsModel) )
```

The final distribution of somas is displayed in figure 6.2 **b**. The lightening in both figures 6.2 **a** and **b** maps the direction perpendicular to the sheet plane. Finally, to add some stochasticity, the election of the morphology for each place was random:

```
NeuronNames = ["I040913C2","n409"]
cells = [ Neuron_class( NeuronNames[ rand>0.5 ],cell) for cell in range(numcells) ]
```

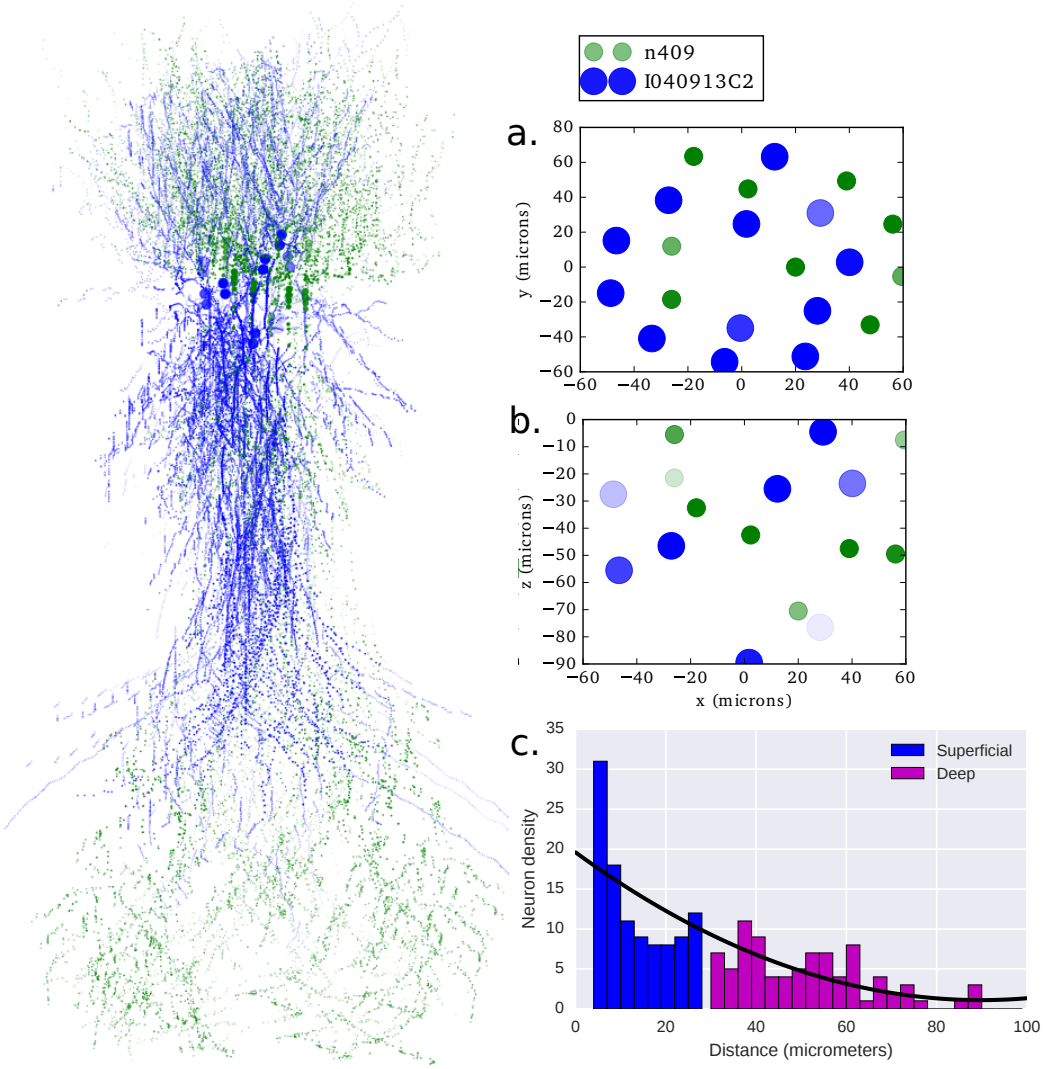

Figure 6.2: **a.** Space distribution of the somas in the $\{x, y\}$ plane. **b.** Space distribution of the somas in the $\{x, z\}$ plane. **c.** Experimental distribution of CA1 PCs from which **b.** is modelled.

In order to estimate simulation workload of adding both cell morphologies and associated compartments to the simulation, an experiment was performed: the simplest morphology was created (one soma and one large apical dendrite), called `BallAndStick` by its accurate description. Figure 6.3 **a** shows the total computational time for 60ms of simulation time, depending on how many compartments had the main apical dendrite of the unique cell. The green line

that fits the data is a quadratic curve:

$$\text{Time} \simeq 10^{-6}\ \texttt{numsegs}^2 + 2 \cdot 10^{-3}\ \texttt{numsegs} + 7 \times 10^{-1}\ \text{(ms)}$$

Figure 6.3**b.** shows the total computational time for 60ms of simulation time depending on how many cells (of 11 compartments) the simulation had. It also has a quadratic time complexity:

$$\text{Time} \simeq 10^{-4}\ \texttt{numcells}^2 + 5 \cdot 10^{-2}\ \texttt{numcells} + -2\ \text{(ms)}$$

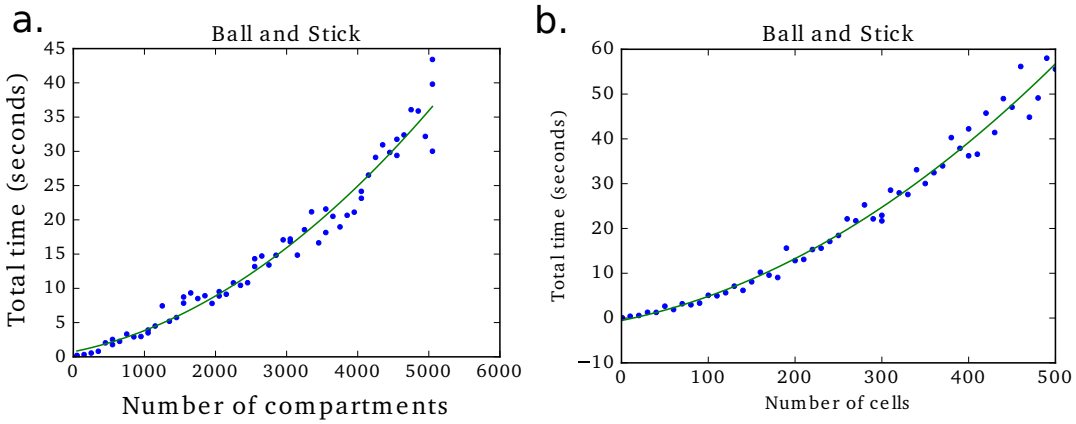

Figure 6.3: **a.** Total computational time for 60ms of simulation time, depending on how many compartments had the main apical dendrite of the unique `BallAndStick` cell. **b.** Total computational time for 60ms of simulation time depending on how many `BallAndStick` cells of 11 compartments the simulation had.

The computer used along the whole work had the following characteristics:

- Operating System: Linux 14.04
- Processors: 4 physical cores with hyperthreading leading to 8 processors, Intel(R) Core(TM) i7-4700MQ CPU model, with a processor speed of 2.40GHz.
- RAM: 16 GB.
- Swap: 32 GB.

The maximal number of simulated neurons was limited by these characteristics. The number of neurons chosen was 20, as they used the whole 16GB of RAM, and almost the 32GB of swap.

6.2.2 Recording LFP signals in the cylinder

Pulse of synapses

We first computed LFP and CSD signals in response to a synaptic input, as in figure 6.1 **b**, but instead using the cylinder of neurons (figure 6.5). At bottom, the firing rate histogram is plotted in green (each cell fire one spike, as seen in figure 5.5). It is noted that neurons did not fire simultaneously, although they were activated by synchronously (`syn_time = 35`). Moreover, differences found in the individual LFP of each morphology are now amplified due to addition of more neurons, and merged because both of morphologies are present.

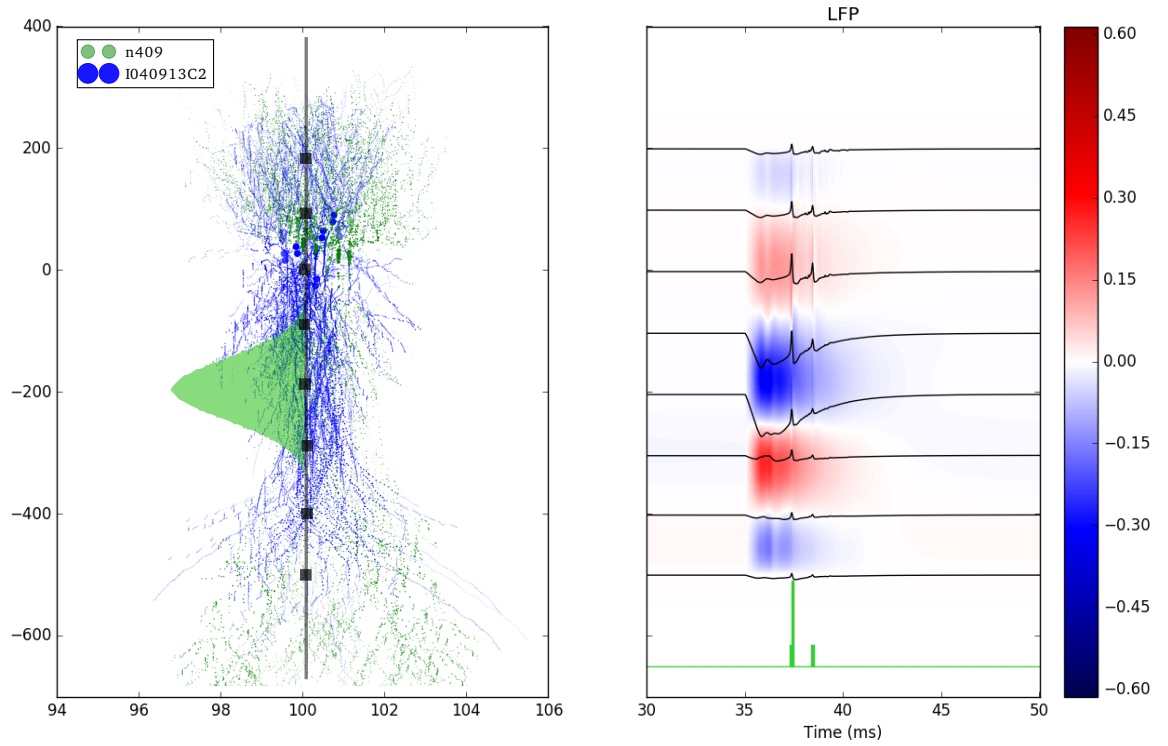

Figure 6.4: LFP of a cylinder of neurons with morphologies I040913C2 and n409 after a 400-synapse pulse.

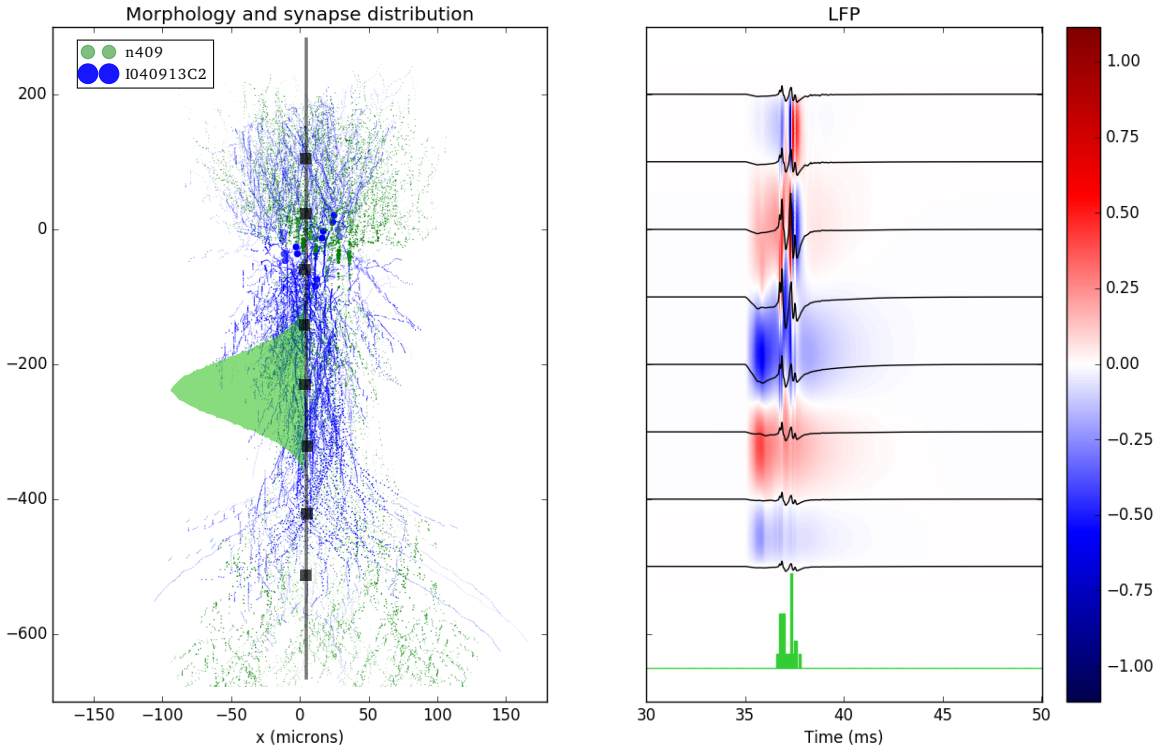

Figure 6.5: LFP of a cylinder of neurons with morphologies I040913C2 and n409 after a 800-synapse pulse.

Theta rhythm

As mentioned before, the main excitatory input of CA1 PCs as Schaffer collaterals from CA3. Theta oscillations brought about CA3 rhythmic excitatory inputs could be modelled by defining the following temporal distribution of synaptic inputs:

$$\mathcal{P}_{\texttt{tsyn}}(t) = \exp\left(\frac{(\mathrm{mod}(t + T_{\mathrm{syn}}\phi, T_{\mathrm{syn}}) - T_{\mathrm{syn}}/2)^2}{2\sigma_{\mathrm{syn}}^2}\right) \tag{6.1}$$

which represents a set of gaussians with mean period $T_{\mathrm{syn}} = 125$ ms and standard deviation $\sigma_{\mathrm{syn}} = T_{\mathrm{syn}}/8$ [Sinha and Narayanan, 2015]. The additional variable ϕ, which is 0 in this case, allow introducing a phase in inputs.

If we define single synaptic release according to this distribution, inputs are not enough to reach the firing threshold. Therefore, more than one release site should be defined for each neuron to fire. Figure 6.6 shows the number of spikes per theta cycle depending on the number of many release sites by cycle in each terminal. Ten theta cycles were simulated for each number of release sites, which are the grey points (darkness indicates number of samples). The mean number of spikes by theta cycle is plotted in colour. As expected, more release sites implies larger firing rate. We chose a value giving roughly 2 spikes/cycle to meet experimental observations. It was set as a parameter, and stored in the `Properties` dictionary:

```
Properties['I040913C2']['ReleaseCycle'] = 30
Properties['n409']['ReleaseCycle'] = 15
```

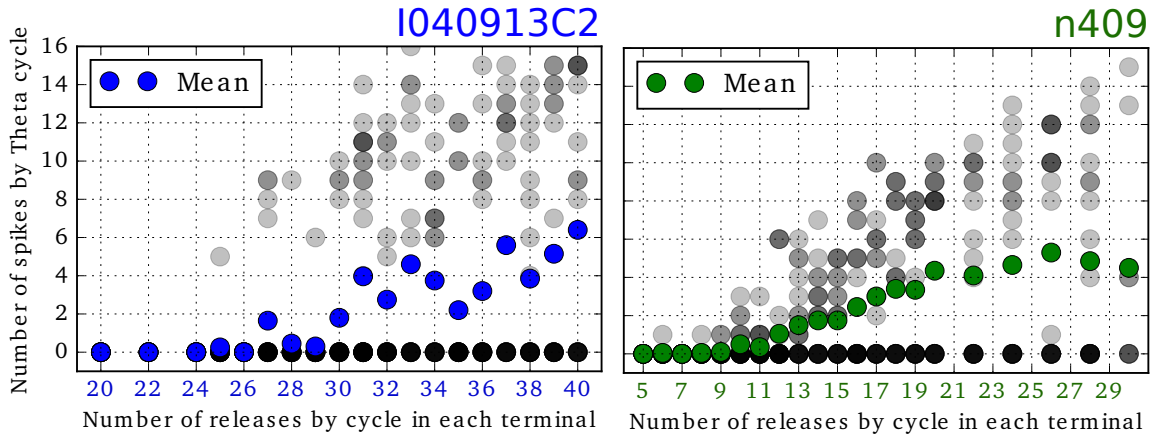

Figure 6.6: Number of spikes by theta cycle depending on number of release sites for morphologies I040913C2 and n409. The mean is shown in color.

Finally, LFP emerging from rhythmic CA3 inputs are shown in figure 6.7. As expected, neuronal firing lumps together at synaptic peaks (see firing histograms at bottom, green). Remarkably, this is consistent with the preferred phase of $\mathrm{PC}_{\mathrm{Sup}}$. However, other experimental features are not reproduced, i.e. theta phase inversion along layers.

A mass effect

These results suggest still a strong individual contribution. For instance, asynchronous firing makes LFP shape illegible and chaotic. A mass effect is needed. With sufficient number of cells, individual contributions may be reduced, while common signals may average. The more neurons

the better the contrast between noise and signal. The best way to achieve a mass effect with current RAM and processors would be to drastically reduce the number of compartments.

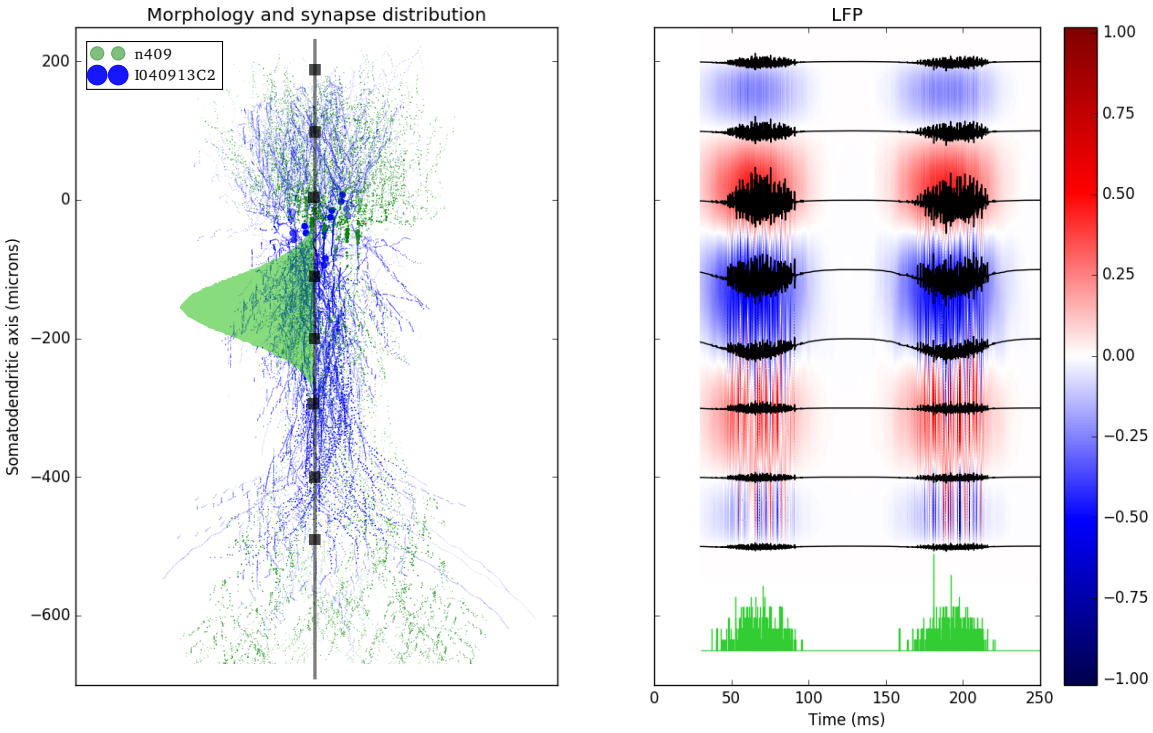

Figure 6.7: LFP of the rhythmic CA3 excitatory input on the cylinder of CA1 PCs

7

Conclusions and future work

In this work, we have successfully simulated activity of individual CA1 PCs for several morphologies, as a pillar for a future realistic model of the CA1 circuitry that includes the most relevant elements involved in the hippocampal theta rhythm.

The following principal biophysical and electrophysiological aspects have been reproduced:

- The effect of morphology on passive properties has been studied using one CA1 pyramidal cell recorded and reconstructed by the host laboratory and three other open-source CA1 neurons collected from NeuroMorpho. The addition of a scale factor to account for the extra surface area due to spines, which depends on both the diameter and the location of the compartment, changed membrane resistance and capacitance in a morphology-dependent way.

- The effect of HCN in neuronal properties was also studied. First, we found HCN influenced the resting membrane potential also in a morphology-dependent form, by depolarizing membranes up to 10 mV on distal compartments. Remarkably, two other effects of HCN channels were sucessfully incorporated: a decrease of EPSP amplitude, and the normalization of somatic EPSP amplitude for independency with synapse location.

- The implementation of active properties required a parametric search. At first, both parameters g_{Na} and g_{K} were set based on the intrinsice response to a current pulse at the soma. The input/output and I/V intrinsic curves were calculated. We found that simulated input resistance matched experimental values for the intracellularly recorded cell. A second parametric study was performed after introducing CA3 synaptic inputs according to a Gaussian-distribution at SR. We examined the role of neuronal morphology and different channel density on the soma and the AIS.

- Addition of the synaptic inputs allowed us to study of the dynamics of EPSP attenuation along the main apical trunk. We focused not only in the effect of HCN, but also on spine scale factors as well as dendritic branching and diameter. These last two factros had differential impact on each compartment, as they indirectly modify the electrotonic length constant, which depends on the diameter.

In a second step of this work, LFP and CSD signals were simulated, first at the level of individual cells and finally to a small cylinder of neurons. We found that:

- Although the morphology-dependence of LFP is notorious, some experimental-like elements were found for individual cell contribution: a sink in the SR next to a source on the SP and the downwards shape of the EPSP field at SR with a phase reversal from SR to SP.
- Thanks to the flexibility of the code, the modelled system was easily escalated and LFP and CSD signals from a cylinder of 20 neurons was generated. The spacial distribution was set according to experimental results of the laboratory. The experimental-like elements mentioned before were still present in the cylinder's LFP for both sub-threshold and supra-threshold responses.
- Finally, rhythmic CA3 synaptic input to SR resulted in an appropiate associated sink at SR with neuronal firing lumped together at synaptic peaks, consistent with the preferred phase of PC_{Sup} .
- In despite of the reduced number of neurons, some basic extracellular features could be reproduced. However, the LFP profile cannot fully matches experimental recordings suggesting the need for a mass effect that limit individual noisy contributions.

This model is by all means a solid mainstay from which to buildup a more realistic simulatio of the CA1 theta rhythm. The conclusions obtained from this work call for future the following improvements:

- To drastically simplify the individual neuronal morphology, preserving their main topology (longitudes, bifurcations, mean diameters...), but reducing the number of compartments. This will allow to proportionally increase the number of neurons in the cylinder and achieving the desired mass effect.
- To add more specific ionic channels that better shape neuronal firing dynamics in a more realistic fashion, including calcium currents, I_M, etc... as well as to refine the parametric searches.
- To add more realistic synaptic inputs from all different sources including deep-superficial differentiation of entorhinal and CA3/CA2 pathways as well as the vast diversity of GABAergic inhibition such as innervation by PVbc and CCKbc interneurons.

Appendix: Code repository

The final version of the latest results can be found in this repository.

(https://github.com/acnavasolive/Computational_Modelling_Deep-Superficial_CA1)

Elements on the repository:

- `/SWC`: folder containing the .swc files from neuron reconstruction. It is important to erase the first commented lines
- ih.mod: NMOD file that controls the HCN channel dynamics
- `LFP_Cylinder_Pulse.py`: A cylinder of the I040913C2 and n409 morphologies is set according to experimental distributions, and the LFP and CSD from a multielectrode array in the central axis of the cilinder after a synapse pulse computed. A .txt with the LFP computation, the membrane voltage of the different somas, and positions from all compartments is saved.
- `LFP_Cyilnder_Theta.py`: A cylinder of the I040913C2 and n409 morphologies is set according to experimental distributions, and the LFP and CSD from a multielectrode array in the central axis of the cilinder after a synapse pulse computed. A .txt with the LFP computation, the membrane voltage of the different somas, and positions from all compartments is saved.
- `LFP_Plot.py`: It plots the LFP and CSD of the .txt saved from the `LFP_Cylinder_- - -.py`.
- `MakePropertiesDictionary.py`: to set the different properties specific for each cell.
- `Properties.pickle`: The dictionary used in the simulation code from where to pick the set properties.

Bibliography

Anant. Agarwal and Jeffrey H. Lang. *6.002 Circuits and Electronics*. Spring, 2007. ISBN 9781558607354. URL https://ocw.mit.edu/courses/electrical-engineering-and-computer-science/6-002-circuits-and-electronics-spring-2007/index.htm.

Paulo Aguiar, Mafalda Sousa, and Peter Szucs. Versatile Morphometric Analysis and Visualization of the Three-Dimensional Structure of Neurons. *Neuroinformatics*, 11(4):393–403, 10 2013. doi: 10.1007/s12021-013-9188-z. URL http://link.springer.com/10.1007/s12021-013-9188-z.

David G Amaral, Norio Ishizuka, and Brenda Claiborne. Neurons, numbers and the hippocampal network. *Progress in brain research*, 83:1–11, 1990. URL http://www.ncbi.nlm.nih.gov/pubmed/2203093.

Costas A. Anastassiou, Sean M. Montgomery, Mauricio Barahona, György Buzsáki, and Christof Koch. The Effect of Spatially Inhomogeneous Extracellular Electric Fields on Neurons. *Journal of Neuroscience*, 30(5), 2010. URL http://www.jneurosci.org/content/30/5/1925.long.

Per. Andersen. *The hippocampus book*. Oxford University Press, 2007. ISBN 0195100271.

Giorgio A. Ascoli, Duncan E. Donohue, and Maryam Halavi. NeuroMorpho.Org. URL http://neuromorpho.org/#.

Giorgio A. Ascoli, Duncan E. Donohue, and Maryam Halavi. NeuroMorpho.Org: A Central Resource for Neuronal Morphologies. *Journal of Neuroscience*, 27(35), 2007. URL http://www.jneurosci.org/content/27/35/9247.

Marianne J. Bezaire and Ivan Soltesz. Quantitative assessment of CA1 local circuits: Knowledge base for interneuron-pyramidal cell connectivity. *Hippocampus*, 23(9):751–785, 2013. ISSN 10509631. doi: 10.1002/hipo.22141.

Kevin Wood Bieri, Katelyn N Bobbitt, and Laura Lee Colgin. Slow and fast γ rhythms coordinate different spatial coding modes in hippocampal place cells. *Neuron*, 82(3):670–81, 5 2014. doi: 10.1016/j.neuron.2014.03.013. URL http://www.ncbi.nlm.nih.gov/pubmed/24746420http://www.ncbi.nlm.nih.gov/pubmed/24746420.

Chris M. Bird and Neil Burgess. The hippocampus and memory: insights from spatial processing. *Nature Reviews Neuroscience*, 9(3):182–194, 3 2008. ISSN 1471-003X. doi: 10.1038/nrn2335. URL http://www.ncbi.nlm.nih.gov/pubmed/18270514http://www.nature.com/doifinder/10.1038/nrn2335.

György Buzsáki. Theta Oscillations in the Hippocampus. *Neuron*, 33(3):325–340, 2002. ISSN 08966273. doi: 10.1016/S0896-6273(02)00586-X. URL http://www.sciencedirect.com/science/article/pii/S089662730200586X.

György Buzsáki and Edvard I Moser. Memory, navigation and theta rhythm in the hippocampal-entorhinal system. *Nature Neuroscience*, 16(2):130–138, 1 2013. doi: 10.1038/nn.3304. URL http://www.ncbi.nlm.nih.gov/pubmed/23354386http://www.ncbi.nlm.nih.gov/pubmed/23354386http://www.ncbi.nlm.nih.gov/pubmed/23354386.

György Buzsáki, Costas A. Anastassiou, and Christof Koch. The origin of extracellular fields and currents — EEG, ECoG, LFP and spikes. *Nature Reviews Neuroscience*, 13(6):407–420, 2012. ISSN 1471-003X. doi: 10.1038/nrn3241. URL http://www.nature.com/doifinder/10.1038/nrn3241.

Nicholas T. Carnevale and Michael L. Hines. *The NEURON Book*. Cambridge University Press, Cambridge, 2006. ISBN 9780511541612. doi: 10.1017/CBO9780511541612. URL http://ebooks.cambridge.org/ref/id/CBO9780511541612.

Bob Eisenberg. Computing the Field in Proteins and Channels. 9 2010. URL http://arxiv.org/abs/1009.2857.

G. Bard Ermentrout and David H. Terman. *Mathematical Foundations of Neuroscience*, volume 35 of *Interdisciplinary Applied Mathematics*. Springer New York, New York, NY, 2010. ISBN 978-0-387-87707-5. doi: 10.1007/978-0-387-87708-2. URL http://link.springer.com/10.1007/978-0-387-87708-2.

Adolf Fick. Ueber Diffusion. *Annalen der Physik und Chemie*, 170(1):59–86, 1855. doi: 10.1002/andp.18551700105. URL http://doi.wiley.com/10.1002/andp.18551700105.

Tamás F Freund. Interneuron Diversity series: Rhythm and mood in perisomatic inhibition. *Trends in Neurosciences*, 26(9):489–495, 9 2003. ISSN 01662236. doi: 10.1016/S0166-2236(03)00227-3. URL http://www.ncbi.nlm.nih.gov/pubmed/12948660http://linkinghub.elsevier.com/retrieve/pii/S0166223603002273.

Tomás F. Freund and György Buzsáki. Interneurons of the hippocampus. *Hippocampus*, 6(4):347–470, 12 1998. doi: 10.1002/(SICI)1098-1063(1996)6:4<347::AID-HIPO1>3.0.CO;2-I. URL http://doi.wiley.com/10.1002/%28SICI%291098-1063%281996%296%3A4%3C347%3A%3AAID-HIPO1%3E3.0.CO%3B2-I.

Keith Godfrey. Compartmental models and their application. *Journal of Pharmaceutical Science: JPharmSc*, 1983. URL http://bases.bireme.br/cgi-bin/wxislind.exe/iah/online/?IsisScript=iah/iah.xis&src=google&base=REPIDISCA&lang=p&nextAction=lnk&exprSearch=134137&indexSearch=ID.

Carl Gold, Darrell A Henze, Christof Koch, and György Buzsáki. On the Origin of the Extracellular Action Potential Waveform : A Modeling Study On the Origin of the Extracellular Action Potential Waveform : A Modeling Study. *J Neurophysiol*, 95:3113–3128, 2006. ISSN 0022-3077. doi: 10.1152/jn.00979.2005.

Maryam Halavi, Kelly A. Hamilton, Ruchi Parekh, and Giorgio A. Ascoli. Digital Reconstructions of Neuronal Morphology: Three Decades of Research Trends. *Frontiers in Neuroscience*, 6, 2012. doi: 10.3389/fnins.2012.00049. URL http://journal.frontiersin.org/article/10.3389/fnins.2012.00049/abstract.

Michael E. Hasselmo, Clara Bodelón, and Bradley P. Wyble. A Proposed Function for Hippocampal Theta Rhythm: Separate Phases of Encoding and Retrieval Enhance Reversal of Prior Learning. *Neural Computation*, 14(4):793–817, 2002. ISSN 0899-7667. doi: 10.1162/089976602317318965. URL http://www.mitpressjournals.org/doi/10.1162/089976602317318965.

Michel E Hasselmo, Eric Schnell, and Edi Barkai. Dynamics of learning and recall at excitatory recurrent synapses and cholinergic modulation in rat hippocampal region CA3. *The Journal of neuroscience : the official journal of the Society for Neuroscience*, 15(7 Pt 2):5249–62, 7 1995. URL http://www.ncbi.nlm.nih.gov/pubmed/7623149.

Bertil Hille. *Ion Channels of Excitable Membranes*. Sinauer Associates is an imprint of Oxford University Press;, Massachusetts, 3 edition, 2001. URL http://www.esalq.usp.br/lepse/imgs/conteudo_thumb/Ion-Channels-of-Excitable-Membranes.pdf.

Michel L. Hines and Ted Carnevale. Neuron: A Tool for Neuroscientists. *The Neuroscientist*, 7(2):123–135, 4 2001. doi: 10.1177/107385840100700207. URL http://www.ncbi.nlm.nih.gov/pubmed/11496923.

Michel L. Hines and Ted Carnevale. NEURON | for empirically-based simulations of neurons and networks of neurons. URL http://neuron.yale.edu/neuron/.

Frederick L. Hitti and Steven A. Siegelbaum. The hippocampal CA2 region is essential for social memory. *Nature*, 508(7494):88–92, 2 2014. doi: 10.1038/nature13028. URL http://www.ncbi.nlm.nih.gov/pubmed/24572357.

Alan Lloyd Hodgkin and Andrew Huxley. A quantitative description of membrane current and its application to conduction and excitation in nerve. *The Journal of physiology*, 117(4):500–44, 8 1952a. URL http://www.ncbi.nlm.nih.gov/pubmed/12991237.

Alan Lloyd Hodgkin and Andrew Huxley. Currents carried by sodium and potassium ions through the membrane of the giant axon of Loligo. *The Journal of physiology*, 116(4):449–72, 4 1952b. URL http://www.ncbi.nlm.nih.gov/pubmed/14946713.

Alan Lloyd Hodgkin and Andrew Huxley. The components of membrane conductance in the giant axon of Loligo. *The Journal of physiology*, 116(4):473–96, 4 1952c. URL http://www.ncbi.nlm.nih.gov/pubmed/14946714.

Alan Lloyd Hodgkin and Andrew Huxley. The dual effect of membrane potential on sodium conductance in the giant axon of Loligo. *The Journal of physiology*, 116(4):497–506, 4 1952d. URL http://www.ncbi.nlm.nih.gov/pubmed/14946715.

Alan Lloyd Hodgkin, Andrew Huxley, and Bernard Katz. Measurement of current-voltage relations in the membrane of the giant axon of Loligo. *The Journal of physiology*, 116(4):424–48, 4 1952. URL http://www.ncbi.nlm.nih.gov/pubmed/14946712.

William R. Holmes and Wilfrid Rall. Electrotonic length estimates in neurons with dendritic tapering or somatic shunt. *Journal of Neurophysiology*, 68(4), 1992. URL http://jn.physiology.org/content/68/4/1421.

Gary R Holt and Christof Koch. Electrical Interactions via the Extracellular Potential Near Cell Bodies. *Journal of Computational Neuroscience*, 6:169–184, 1999. URL http://icslwebs.ee.ucla.edu/dejan/researchwiki/images/3/31/Holt99.pdf.

John J Hopfield. Neural networks and physical systems with emergent collective computational abilities. *Proceedings of the National Academy of Sciences*, 79:2554–2558, 1982. URL http://www.pnas.org/content/79/8/2554.full.pdf.

J. M. Ibarz, G. Foffani, E. Cid, M. Inostroza, and L. Menendez de la Prida. Emergent Dynamics of Fast Ripples in the Epileptic Hippocampus. *Journal of Neuroscience*, 30(48):16249–16261, 2010. ISSN 0270-6474. doi: 10.1523/JNEUROSCI.3357-10.2010. URL http://www.jneurosci.org/cgi/doi/10.1523/JNEUROSCI.3357-10.2010.

Dieter Jaeger and Ranu Jung. *Encyclopedia of Computational Neuroscience.* Springer Verlag, 2014. ISBN 9781461466765.

Anita Kamondi, László Acsády, Xiao-Jing Wang, and György Buzsáki. Theta oscillations in somata and dendrites of hippocampal pyramidal cells in vivo: activity-dependent phase-precession of action potentials. *Hippocampus*, 8(3):244–61, 1998. doi: 10.1002/(SICI)1098-1063(1998)8:3{\&}lt;244::AID-HIPO7{\&}gt;3.0.CO;2-J. URL http://www.ncbi.nlm.nih.gov/pubmed/9662139.

Thomas Klausberger and Peter Somogyi. Neuronal diversity and temporal dynamics: the unity of hippocampal circuit operations. *Science (New York, N.Y.)*, 321(5885):53–7, 7 2008. doi: 10.1126/science.1149381. URL http://www.ncbi.nlm.nih.gov/pubmed/18599766.

Thomas Klausberger, Peter J. Magill, László F. Márton, J. David B. Roberts, Philip M. Cobden, György Buzsáki, and Peter Somogyi. Brain-state- and cell-type-specific firing of hippocampal interneurons in vivo. *Nature*, 421(6925):844–848, 2 2003. doi: 10.1038/nature01374. URL http://www.ncbi.nlm.nih.gov/pubmed/12594513http://www.ncbi.nlm.nih.gov/pubmed/12594513.

Toshio Kosaka, Hironobu Katsumaru, Kiyoshi Hama, Jang-Yen Wu, and Claus W Heizmann. GABAergic neurons containing the Ca2+-binding protein parvalbumin in the rat hippocampus and dentate gyrus. *Brain research*, 419(1-2):119–30, 9 1987. URL http://www.ncbi.nlm.nih.gov/pubmed/3315112.

Brett Lancaster and Paul R Adams. Calcium-dependent current generating the afterhyperpolarization of hippocampal neurons. *Journal of neurophysiology*, 55(6):1268–82, 6 1986. URL http://www.ncbi.nlm.nih.gov/pubmed/2426421.

Brett Lancaster and Roger A Nicoll. Properties of two calcium-activated hyperpolarizations in rat hippocampal neurones. *The Journal of physiology*, 389:187–203, 8 1987. URL http://www.ncbi.nlm.nih.gov/pubmed/2445972http://www.ncbi.nlm.nih.gov/pubmed/2445972.

Sang-Hun Lee, Ivan Marchionni, Marianne Bezaire, Csaba Varga, Nathan Danielson, Matthew Lovett-Barron, Attila Losonczy, and Ivan Soltesz. Parvalbumin-Positive Basket Cells Differentiate among Hippocampal Pyramidal Cells. *Neuron*, 82(5):1129–1144, 6 2014. doi: 10.1016/j.neuron.2014.03.034. URL http://www.ncbi.nlm.nih.gov/pubmed/24836505.

Jill K. Leutgeb, Stefan Leutgeb, May-Britt Moser, and Edvard I. Moser. Pattern Separation in the Dentate Gyrus and CA3 of the Hippocampus. *Science*, 315(5814):961–966, 2 2007. doi: 10.1126/science.1135801. URL http://www.ncbi.nlm.nih.gov/pubmed/17303747.

Rodolfo R. Llinás. The intrinsic electrophysiological properties of mammalian neurons: insights into central nervous system function. *Science (New York, N.Y.)*, 242(4886):1654–64, 12 1988. URL http://www.ncbi.nlm.nih.gov/pubmed/3059497.

Laura López-Aguado, José Manuel Ibarz, and Oscar Herreras. Activity-dependent changes of tissue resistivity in the CA1 region in vivo are layer-specific: modulation of evoked potentials. *Neuroscience*, 108(2):249–62, 2001. URL http://www.ncbi.nlm.nih.gov/pubmed/11734358.

Laura Lopez-Aguado, José Manuel Ibarz, Pablo Varona, and Oscar Herreras. Structural Inhomogeneities Differentially Modulate Action Currents and Population Spikes Initiated in the Axon or Dendrites. *Journal of Neurophysiology*, 88(5):2809–2820, 11 2002. doi: 10.1152/jn.00183.2002. URL http://www.ncbi.nlm.nih.gov/pubmed/12424314.

Rafael Lorente de Nó. *Studies on the structure of the cerebral cortex.* Johann Ambrosius Barth, Leipzig, 1934. URL http://www.worldcat.org/title/studies-on-the-structure-of-the-cerebral-cortex-ii-continuation-of-the-study-of-the-ammoni oclc/665048285.

Vincenzo Macri, Damiano Angoli, and Eric A. Accili. Architecture of the HCN selectivity filter and control of cation permeation. *Scientific Reports*, 2, 11 2012. doi: 10.1038/srep00894. URL http://www.nature.com/articles/srep00894.

Jeffrey C Magee. Dendritic hyperpolarization-activated currents modify the integrative properties of hippocampal CA1 pyramidal neurons. *The Journal of neuroscience : the official journal of the Society for Neuroscience*, 18(19):7613–24, 10 1998. URL http://www.ncbi.nlm.nih.gov/pubmed/9742133.

Jeffrey C. Magee. Dendritic lh normalizes temporal summation in hippocampal CA1 neurons. *Nature Neuroscience*, 2(6):508–514, 6 1999. doi: 10.1038/9158. URL http://www.ncbi.nlm.nih.gov/pubmed/10448214.

Jeffrey C Magee and Daniel Johnston. Characterization of single voltage-gated Na+ and Ca2+ channels in apical dendrites of rat CA1 pyramidal neurons. *The Journal of physiology*, 487 (1):67–90, 8 1995. URL http://www.ncbi.nlm.nih.gov/pubmed/7473260.

Arjun V. Masurkar, Kalyan V. Srinivas, David H. Brann, Richard Warren, Daniel C. Lowes, and Steven A. Siegelbaum. Medial and Lateral Entorhinal Cortex Differentially Excite Deep versus Superficial CA1 Pyramidal Neurons. *Cell Reports*, 18(1):148–160, 1 2017. ISSN 22111247. doi: 10.1016/j.celrep.2016.12.012. URL http://linkinghub.elsevier.com/retrieve/pii/S2211124716316850.

Chris J McBain, Timothy J DiChiara, and Julie A Kauer. Activation of metabotropic glutamate receptors differentially affects two classes of hippocampal interneurons and potentiates excitatory synaptic transmission. *The Journal of neuroscience : the official journal of the Society for Neuroscience*, 14(7):4433–45, 7 1994. URL http://www.ncbi.nlm.nih.gov/pubmed/7517996.

George Meena S, L F Abbott, and Steven A Siegelbaum. HCN hyperpolarization-activated cation channels inhibit EPSPs by interactions with M-type K+ channels. *Nature Neuroscience*, 12 (5):577–584, 5 2009. doi: 10.1038/nn.2307. URL http://www.nature.com/doifinder/10.1038/nn.2307.

Manuel Megías, Zsuzsa S., Tamás F. Freund, and Attila I. Gulyás. Total number and distribution of inhibitory and excitatory synapses on hippocampal CA1 pyramidal cells. *Neuroscience*, 102 (3):527–540, 2001. doi: 10.1016/S0306-4522(00)00496-6. URL http://www.sciencedirect.com/science/article/pii/S0306452200004966.

Kenji Mizuseki, Anton Sirota, Eva Pastalkova, and György Buzsáki. Theta oscillations provide temporal windows for local circuit computation in the entorhinal-hippocampal loop. *Neuron*, 64(2):267–80, 10 2009. ISSN 1097-4199. doi: 10.1016/j.neuron.2009.08.037. URL http://www.ncbi.nlm.nih.gov/pubmed/19874793http://www.pubmedcentral.nih.gov/articlerender.fcgi?artid=PMC2771122.

Kenji Mizuseki, Kamran Diba, Eva Pastalkova, and György Buzsáki. Hippocampal CA1 pyramidal cells form functionally distinct sublayers. *Nature Neuroscience*, 14(9):1174–1181, 8 2011. doi: 10.1038/nn.2894. URL http://www.ncbi.nlm.nih.gov/pubmed/21822270.

Sean M Montgomery and György Buzsáki. Gamma oscillations dynamically couple hippocampal CA3 and CA1 regions during memory task performance. *Proceedings of the National*

Academy of Sciences of the United States of America, 104(36):14495–500, 9 2007. doi: 10.1073/pnas.0701826104. URL http://www.ncbi.nlm.nih.gov/pubmed/17726109http://www.ncbi.nlm.nih.gov/pubmed/17726109.

Rishikesh Narayanan and Sumantra Chattarji. Computational analysis of the impact of chronic stress on intrinsic and synaptic excitability in the hippocampus. *Journal of neurophysiology*, 103(6):3070–83, 6 2010. doi: 10.1152/jn.00913.2009. URL http://www.ncbi.nlm.nih.gov/pubmed/20457854http://www.ncbi.nlm.nih.gov/pubmed/20457854.

Joshua P. Neunuebel and James J. Knierim. CA3 Retrieves Coherent Representations from Degraded Input: Direct Evidence for CA3 Pattern Completion and Dentate Gyrus Pattern Separation. *Neuron*, 81(2):416–427, 1 2014. doi: 10.1016/j.neuron.2013.11.017. URL http://www.ncbi.nlm.nih.gov/pubmed/24462102.

Georg Simon Ohm. *Die galvanische kette, mathematisch*. Berlin, T. H. Riemann, 1827. URL https://archive.org/details/diegalvanischek00ohmgoog.

John O'Keefe and Michael L. Recce. Phase relationship between hippocampal place units and the EEG theta rhythm. *Hippocampus*, 3(3):317–330, 7 1993. ISSN 1050-9631. doi: 10.1002/hipo.450030307. URL http://doi.wiley.com/10.1002/hipo.450030307.

Randall C. O'Reilly and James L. McClelland. Hippocampal conjunctive encoding, storage, and recall: Avoiding a trade-off. *Hippocampus*, 4(6):661–682, 12 1994. doi: 10.1002/hipo.450040605. URL http://www.ncbi.nlm.nih.gov/pubmed/7704110.

Hanchuan Peng, Zongcai Ruan, Fuhui Long, Julie H Simpson, and Eugene W Myers. V3D enables real-time 3D visualization and quantitative analysis of large-scale biological image data sets. *Nature Biotechnology*, 28(4):348–353, 4 2010. doi: 10.1038/nbt.1612. URL http://www.nature.com/doifinder/10.1038/nbt.1612.

Hanchuan Peng, Jianyong Tang, Hang Xiao, Alessandro Bria, Jianlong Zhou, Victoria Butler, Zhi Zhou, Paloma T. Gonzalez-Bellido, Seung W. Oh, Jichao Chen, Ananya Mitra, Richard W. Tsien, Hongkui Zeng, Giorgio A. Ascoli, Giulio Iannello, Michael Hawrylycz, Eugene Myers, and Fuhui Long. Virtual finger boosts three-dimensional imaging and microsurgery as well as terabyte volume image visualization and analysis. *Nature Communications*, 5, 7 2014. doi: 10.1038/ncomms5342. URL http://www.nature.com/doifinder/10.1038/ncomms5342.

Dale Purves, George J Augustine, David Fitzpatrick, Lawrence C Katz, Anthony-Samuel LaMantia, James O McNamara, and S Mark Williams. *Neuroscience*. Sinauer Associates, 2 edition, 2001. URL https://www.ncbi.nlm.nih.gov/books/NBK11117/.

Gowri K. Pyapali, Attila Sik, Markku Penttonen, György Buzsaki, and Dennis A. Turner. Dendritic properties of hippocampal CA1 pyramidal neurons in the rat: Intracellular staining in vivo and in vitro. *The Journal of Comparative Neurology*, 391(3):335–352, 2 1998. doi: 10.1002/(SICI)1096-9861(19980216)391:3<335::AID-CNE4>3.0.CO;2-2. URL http://doi.wiley.com/10.1002/%28SICI%291096-9861%2819980216%29391%3A3%3C335%3A%3AAID-CNE4%3E3.0.CO%3B2-2.

Wilfrid Rall. Time Constants and Electrotonic Length of Membrane Cylinders and Neurons. *Biophysical Journal*, 9(12):1483–1508, 12 1969. doi: 10.1016/S0006-3495(69)86467-2. URL http://linkinghub.elsevier.com/retrieve/pii/S0006349569864672.

Wilfrid Rall and Gordon M Shepherd. Theoretical reconstruction of field potentials and dendrodendritic synaptic interactions in olfactory bulb. *Journal of neurophysiology*, 31(6):884–915, 11 1968. URL http://www.ncbi.nlm.nih.gov/pubmed/5710539.

Saikat Ray, Robert Naumann, Andrea Burgalossi, Qiusong Tang, Helene Schmidt, and Michael Brecht. Grid-Layout and Theta-Modulation of Layer 2 Pyramidal Neurons in Medial Entorhinal Cortex. *Science*, 343(6173):891–896, 2 2014. doi: 10.1126/science.1243028. URL http://www.ncbi.nlm.nih.gov/pubmed/24457213.

Alfredo Rodriguez, Douglas B. Ehlenberger, Dara L. Dickstein, Patrick R. Hof, and Susan L. Wearne. Automated Three-Dimensional Detection and Shape Classification of Dendritic Spines from Fluorescence Microscopy Images. *PLoS ONE*, 3(4):e1997, 4 2008. doi: 10.1371/journal.pone.0001997. URL http://dx.plos.org/10.1371/journal.pone.0001997.

Brandy N. Routh, Daniel Johnston, Kristen Harris, and Raymond A. Chitwood. Anatomical and Electrophysiological Comparison of CA1 Pyramidal Neurons of the Rat and Mouse. *Journal of Neurophysiology*, 102(4):2288–2302, 10 2009. doi: 10.1152/jn.00082.2009. URL http://www.ncbi.nlm.nih.gov/pubmed/19675296.

Karl Schaffer. Beitrag zur Histologie der Ammonshornformation. *Archiv für Mikroskopische Anatomie*, 39(1):611–632, 12 1892. ISSN 0176-7364. doi: 10.1007/BF02961541. URL http://link.springer.com/10.1007/BF02961541.

Erik W Schomburg, Costas A Anastassiou, György Buzsáki, and Christof Koch. The spiking component of oscillatory extracellular potentials in the rat hippocampus. *The Journal of neuroscience : the official journal of the Society for Neuroscience*, 32(34):11798–811, 8 2012. doi: 10.1523/JNEUROSCI.0656-12.2012. URL http://www.ncbi.nlm.nih.gov/pubmed/22915121http://www.ncbi.nlm.nih.gov/pubmed/22915121.

Philip A Schwartzkroin. Characteristics of CA1 neurons recorded intracellularly in the hippocampal in vitro slice preparation. *Brain research*, 85(3):423–36, 3 1975. URL http://www.ncbi.nlm.nih.gov/pubmed/1111846.

William B Scoville and Brenda Milner. Loss of recent memory after bilateral hippocampal lesions. *Journal of neurology, neurosurgery, and psychiatry*, 20(1):11–21, 2 1957. URL http://www.ncbi.nlm.nih.gov/pubmed/13406589.

Mala M. Shah. Recording Dendritic Ion Channel Properties and Function from Cortical Neurons. In *Methods in molecular biology (Clifton, N.J.)*, volume 998, pages 303–309. 2013. doi: 10.1007/978-1-62703-351-0{_}24. URL http://www.ncbi.nlm.nih.gov/pubmed/23529440http://www.ncbi.nlm.nih.gov/pubmed/23529440.

Li-Rong Shao, Ragnhild Halvorsrud, Lyle Borg-Graham, and Johan F. Storm. The role of BK-type Ca ²⁺ -dependent K ⁺ channels in spike broadening during repetitive firing in rat hippocampal pyramidal cells. *The Journal of Physiology*, 521 (1):135–146, 11 1999. doi: 10.1111/j.1469-7793.1999.00135.x. URL http://doi.wiley.com/10.1111/j.1469-7793.1999.00135.x.

Manisha Sinha and Rishikesh Narayanan. HCN channels enhance spike phase coherence and regulate the phase of spikes and LFPs in the theta-frequency range. *Proceedings of the National Academy of Sciences*, 112(17):E2207–E2216, 2015. ISSN 0027-8424. doi: 10.1073/pnas.1419017112. URL http://www.pnas.org/lookup/doi/10.1073/pnas.1419017112.

Micha E. Spira and Aviad Hai. Multi-electrode array technologies for neuroscience and cardiology. *Nature Nanotechnology*, 8(2):83–94, 2 2013. ISSN 1748-3387. doi: 10.1038/nnano.2012.265. URL http://www.nature.com/doifinder/10.1038/nnano.2012.265.

Nelson Spruston. Pyramidal neurons: dendritic structure and synaptic integration. *Nature Reviews Neuroscience*, 9(3):206–221, 3 2008. ISSN 1471-003X. doi: 10.1038/nrn2286. URL http://www.nature.com/doifinder/10.1038/nrn2286.

Kalyan V. Srinivas, Eric W. Buss, Qian Sun, Bina Santoro, Hiroto Takahashi, Daniel A. Nicholson, and Steven A. Siegelbaum. The Dendrites of CA2 and CA1 Pyramidal Neurons Differentially Regulate Information Flow in the Cortico-Hippocampal Circuit. *The Journal of Neuroscience*, 37(12):3276–3293, 2017. ISSN 0270-6474. doi: 10.1523/JNEUROSCI.2219-16.2017. URL `http://www.jneurosci.org/lookup/doi/10.1523/JNEUROSCI.2219-16.2017`.

The Scipy community. Python object serialization, pickle. URL `https://docs.python.org/2/library/pickle.html`.

Andrew J. Trevelyan. The Direct Relationship between Inhibitory Currents and Local Field Potentials. *Journal of Neuroscience*, 29(48):15299–15307, 12 2009. doi: 10.1523/JNEUROSCI.2019-09.2009. URL `http://www.ncbi.nlm.nih.gov/pubmed/19955382`.

Manuel Valero, Elena Cid, Robert G Averkin, Juan Aguilar, Alberto Sanchez-Aguilera, Tim J Viney, Daniel Gomez-Dominguez, Elisa Bellistri, and Liset Menendez de la Prida. Determinants of different deep and superficial CA1 pyramidal cell dynamics during sharp-wave ripples. *Nature Neuroscience*, 18(9):1281–1290, 2015. ISSN 1097-6256. doi: 10.1038/nn.4074. URL `http://www.nature.com/doifinder/10.1038/nn.4074`.

Csaba Varga, Soo Yeun Lee, and Ivan Soltesz. Target-selective GABAergic control of entorhinal cortex output. *Nature Neuroscience*, 13(7):822–824, 7 2010. doi: 10.1038/nn.2570. URL `http://www.ncbi.nlm.nih.gov/pubmed/20512133`.

Matthew J Wayner and Raimond Emmers. Spinal synaptic delay in young and aged rats. *The American journal of physiology*, 194(2):403–5, 8 1958. URL `http://www.ncbi.nlm.nih.gov/pubmed/13559488`.

Frank H Yu and William A Catterall. Overview of the voltage-gated sodium channel family. *Genome biology*, 4(3):207, 2003. URL `http://www.ncbi.nlm.nih.gov/pubmed/12620097`.

Li-Lian Yuan and Xixi Chen. Diversity of potassium channels in neuronal dendrites. *Progress in Neurobiology*, 78(6):374–389, 2006. doi: 10.1016/j.pneurobio.2006.03.003. URL `http://www.sciencedirect.com/science/article/pii/S030100820600027X`.